

MULTISCALE NEURAL NETWORKS FOR APPROXIMATING GREEN'S FUNCTIONS

WENRUI HAO*, RUI PENG LI[†], YUANZHE XI[‡], TIANSHI XU[‡], AND YAHONG YANG*

Abstract. Neural networks (NNs) have been widely used to solve partial differential equations (PDEs) in the applications of physics, biology, and engineering. One effective approach for solving PDEs with a fixed differential operator is learning Green's functions. However, Green's functions are notoriously difficult to learn due to their poor regularity, which typically requires larger NNs and longer training times. In this paper, we address these challenges by leveraging multiscale NNs to learn Green's functions. Through theoretical analysis using multiscale Barron space methods and experimental validation, we show that the multiscale approach significantly reduces the necessary NN size and accelerates training.

Key words. Green's function, Barron space, multiscale neural networks, PDEs, domain decomposition, fast solver

AMS subject classifications. 65N55, 65N80, 68T07

1. Introduction. In recent years, the application of neural networks (NNs) to solving Partial Differential Equations (PDEs) has spurred the development of a range of innovative methodologies. These methods can generally be classified into two main categories: function learning and operator learning. The function learning methods, such as Physics-Informed NNs (PINNs) [43], the Deep Ritz Method [15], the Deep Galerkin Method [50], and approaches based on random features [8, 11, 51], utilize NNs to directly approximate the solutions of PDEs using specifically designed loss functions.

A significant limitation of the function learning approaches is the need to train a separate NN for each PDE if it differs from the one the network was originally trained on. On the other hand, the operator learning methods, such as DeepONet [35] and Fourier Neural Operator (FNO) [30], focus on learning the operator that maps between the PDE parameters and their corresponding solutions. These methods are more general and do not require retraining for different PDEs, provided that the differential operator remains unchanged. However, the challenges of operator learning lie in handling mappings between infinite-dimensional spaces, which pose significant learning difficulties for NNs. To address these issues, we consider Green's function methods for solving PDEs in this paper as this approach does not require retraining the NN when the source function changes.

Although there are many methods for solving PDEs via neural network structures, training remains one of the most difficult parts. The reason is that the loss function for neural networks is non-convex, making it challenging to find the global minimum. Several methods have been developed to reduce these training complexities. One approach fixes the nonlinear part and solves only the linear parameters, known as the random feature model method [8, 11, 51]. Another approach involves initially finding the global minimum for a simpler neural network and then gradually smoothly increasing the network complexity. This is referred to as the greedy algorithm [47] or the homotopy method [60, 66]. Another technique is to divide the neural network into several parts (stacking several simple neural networks) and train the simpler networks one by one to achieve the overall goal. Alternatively, optimizing the direction of gradient descent can improve the training dynamics, as discussed in [2, 27]. Adam [28] or SGD are frequently employed to address the resulting optimization problems in both variational and L_2 -minimization frameworks. Furthermore, methods like Gauss-Newton and Newton type methods have been adapted to train the neural networks [9, 20, 22]. Lastly, using better datasets or applying known data with different levels of fidelity properly can enhance training performance [25]. While various methods exist to improve training performance for solving PDEs, training Green's functions presents unique challenges. Their low regularity and the presence of multiple scales make it difficult to design a neural network capable of effectively learning them. Further details will be provided in the following sections of the paper.

*Department of Mathematics, The Pennsylvania State University, University Park, State College, PA, USA, (wxh64@psu.edu, yxy5498@psu.edu). Research supported by National Institute of General Medical Sciences through grant 1R35GM146894.

[†]Center for Applied Scientific Computing, Lawrence Livermore National Laboratory, P. O. Box 808, L-561, Livermore, CA 94551 (li500@llnl.gov). This work was performed under the auspices of the U.S. Department of Energy by Lawrence Livermore National Laboratory under Contract DE-AC52-07NA27344 (LLNL-JRNL-870805) and was supported by the LLNL-LDRD program under Project No. 24-ERD-033.

[‡]Department of Mathematics, Emory University, Atlanta, GA, USA, (yxi26@emory.edu, tianshi.xu@emory.edu). Research supported by NSF DMS-2338904 and LLNL-LDRD program under Project No. 24-ERD-033.

In particular, we consider the linear PDEs in the following form:

$$(1.1) \quad \begin{cases} \mathcal{L}u(\mathbf{x}) = g_1(\mathbf{x}), & \mathbf{x} \in \Omega \\ \mathcal{B}u(\mathbf{x}) = g_2(\mathbf{x}), & \mathbf{x} \in \partial\Omega \end{cases}$$

where Ω and $\partial\Omega$ are the domain and the domain boundary respectively, $g_1(\mathbf{x})$ and $g_2(\mathbf{x})$ are functions in \mathbb{R} , $u : \mathbb{R}^d \rightarrow \mathbb{R}$, \mathcal{L} is a linear differential operator, and \mathcal{B} is the operator for specifying appropriate boundary conditions (BCs). For impulse source point $\mathbf{y} \in \Omega$, the Green's function $G(\mathbf{x}, \mathbf{y})$ satisfies the following equations:

$$(1.2) \quad \begin{cases} \mathcal{L}G(\mathbf{x}, \mathbf{y}) = \delta(\mathbf{x} - \mathbf{y}), & \mathbf{x} \in \Omega \\ \mathcal{B}G(\mathbf{x}, \mathbf{y}) = 0, & \mathbf{x} \in \partial\Omega \end{cases}$$

where $\delta(\mathbf{x})$ denotes the Dirac delta function:

$$\delta(\mathbf{x}) = \begin{cases} 0, & \mathbf{x} \neq \mathbf{0} \\ \infty, & \mathbf{x} = \mathbf{0} \end{cases} \quad \text{and} \quad \int_{\mathbb{R}^d} \delta(\mathbf{x}) d\mathbf{x} = 1,$$

and both \mathcal{B} and \mathcal{L} operate on the \mathbf{x} variable only. Once $G(\mathbf{x}, \mathbf{y})$ in (1.2) is known, the solution u in (1.1) can be easily computed by the integration of G with arbitrary forcing terms and BCs, g_1 and g_2 .

Deriving analytical expressions for Green's functions is challenging in most cases, even for simple domains, whereas NNs can be promising for approximating Green's functions. Despite Green's functions having twice the dimensionality of the input domain, the same NN model can be effectively applied across different forcing terms without requiring retraining. This approach represents a specialized form of operator learning or an adaptive extension of PINNs that accommodates variations in forcing terms and BCs. Recently, many approaches have been proposed for efficient learning of Green's functions. In [18], the authors establish a framework to learn Green's functions to solve PDEs, but they do not consider the regularity issues that bring difficulties in training. In [31], fundamental solutions are used to address the regularity problem for learning Green's functions; however, for most PDEs, the fundamental solution is unknown. In [26], more complex NNs, such as U-net, are used for training Green's functions. Additionally, in [53], the domain is divided into several parts to reduce training complexity. In [7], the authors focus on sampling strategies to learn Green's functions rather than the structure of NNs. In [55, 65], the authors consider using the Green's function structure to learn the solution of a PDE but do not learn the Green's functions directly.

The primary challenge in Green's function learning approach stems from the low regularity of Green's functions due to the poor regularity of the δ function [16]. For example, the Green's function for the Poisson equation on the unit ball in \mathbb{R}^d has the explicit form:

$$G(\mathbf{x}, \mathbf{y}) = \Phi(\mathbf{y} - \mathbf{x}) - \Phi(\|\mathbf{x}\|_2(\mathbf{y} - \bar{\mathbf{x}})),$$

where Φ is the fundamental solution, $\mathbf{x}, \mathbf{y} \in B_{1, \|\cdot\|_2}$, $B_{r, \|\cdot\|_2}(\mathbf{x}) \subset \mathbb{R}^d$ denotes a closed ball centered at $\mathbf{x} \in \mathbb{R}^d$ with radius r , measured in the Euclidean distance, and $\bar{\mathbf{x}} = \mathbf{x}/\|\mathbf{x}\|_2^2$. It is straightforward to observe that $G(\mathbf{x}, \mathbf{y})$ has singularities at $\mathbf{x} = \mathbf{y}$ as Φ itself is singular at $\mathbf{0}$.

In the approximation theory of NNs [62, 63, 64], the approximation rate can be expressed as $\mathcal{O}(\|G\|_{W^{s, \infty}(\Omega \times \Omega)} N^{-s/d})$, where N is the number of parameters, $\|\cdot\|_{W^{s, \infty}(\Omega \times \Omega)}$ denotes the Sobolev norm [16], and s is the regularity of the target functions. When the target function has lower regularity, meaning that s is small and $\|G\|_{W^{s, \infty}(\Omega \times \Omega)}$ is large, N must be significantly large to achieve a small approximation error. The results in [15, 19, 34, 39, 49] further indicate that a large Sobolev norm of the target functions not only necessitates a large number of parameters but also increases the overall training complexity. This phenomenon has also been examined in generalization analysis, which shows that as the number of parameters increases, the complexity of networks also grows. This increased complexity demands more sample points for effective learning, thereby further escalating the overall training complexity [44, 52, 61]. Thus, target functions with low regularity, such as Green's functions, necessitate a larger number of NN parameters. This, in turn, increases both the training complexity and the data requirements. Another challenge in learning Green's functions is their multiscale nature. Specifically, near $\mathbf{x} = \mathbf{y}$, the Green's function exhibits low regularity, while outside this region, it demonstrates a high-regularity structure [6]. This disparity in regularity makes training

neural networks difficult [23]. When a function involves two distinct regularity scales, and the neural network's initial parameters are tuned to one scale, the network can take significantly longer to learn the low-regularity regions [32, 54, 67].

A common practice in Green's function learning is to first approximate the δ function with a multidimensional Gaussian [1], i.e.,

$$(1.3) \quad \delta(\mathbf{x} - \mathbf{y}) \approx \mathcal{N}_\varepsilon(\mathbf{x}, \mathbf{y}) = \left(\frac{1}{\varepsilon \sqrt{\pi}} \right)^d \exp \left(-\frac{\|\mathbf{x} - \mathbf{y}\|_2^2}{\varepsilon^2} \right),$$

from which we approximate (1.2) as

$$(1.4) \quad \begin{cases} \mathcal{L}G_\varepsilon(\mathbf{x}, \mathbf{y}) = \mathcal{N}_\varepsilon(\mathbf{x}, \mathbf{y}), & \mathbf{x} \in \Omega \\ \mathcal{B}G_\varepsilon(\mathbf{x}, \mathbf{y}) = 0, & \mathbf{x} \in \partial\Omega \end{cases}$$

where ε must be carefully chosen to achieve a good approximation accuracy. Nevertheless, the right-hand side term $\mathcal{N}_\varepsilon(\mathbf{x}, \mathbf{y})$ still exhibits poor regularity.

In this paper, we propose a *multiscale* NN (MSNN) approach designed to fully exploit the multiscale structure inherent in Green's functions. For related work in the literature on MSNN, see e.g., [17, 32, 40, 54]. *The basic idea in our approach is to utilize two NNs at different scales:* one to address the low regularity of $G(\mathbf{x}, \mathbf{y})$ near $\mathbf{x} = \mathbf{y}$, while a second one approximates $G(\mathbf{x}, \mathbf{y})$ across the entire domain. More specifically, the MSNN, denoted by $\phi(\mathbf{z}, \boldsymbol{\theta})$ with $\mathbf{z} = (\mathbf{x}, \mathbf{y})$, consists of two components:

$$(1.5) \quad \phi(\mathbf{z}; \boldsymbol{\theta}) = \frac{1}{n} \sum_{i=1}^n a_i \sigma_\varepsilon(\mathbf{w}_i \cdot \mathbf{z} + b_i) + \frac{1}{m} \sum_{i=n+1}^{n+m} a_i \sigma(\mathbf{w}_i \cdot \mathbf{z} + b_i) + c \equiv \phi_1(\mathbf{z}; \boldsymbol{\theta}_1) + \phi_2(\mathbf{z}, \boldsymbol{\theta}_2)$$

where $\boldsymbol{\theta} = \{a_i\}_{i=1}^{m+n} \cup \{b_i\}_{i=1}^{m+n} \cup \{\mathbf{w}_i\}_{i=1}^{m+n} \cup \{c\}$ are the parameters associated with the $m+n$ neurons and c is combined from the output biases from both ϕ_1 and ϕ_2 . What distinguishes the two components of MSNN is the use of different activation functions, for which we have

$$(1.6) \quad \sigma_\varepsilon(\mathbf{x}) := \varepsilon^\alpha \sigma \left(\frac{\mathbf{x}}{\varepsilon^\beta} \right),$$

with the parameters α, β depending on the PDEs, and ε is the same in (1.3). This network structure introduces two distinct scales within the MSNN.

Following the terminology commonly used in MSNN, we refer to $\phi_1(\mathbf{z}; \boldsymbol{\theta}_1)$ as the *large-scale* NN, which is designed to capture the low regularity of the Green's function near $\mathbf{x} = \mathbf{y}$. On the other hand, $\phi_2(\mathbf{z}; \boldsymbol{\theta}_2)$ is the *small-scale* NN, which instead focuses on learning the smooth regions of the Green's function and the residual of the first part. Recent studies have shown that relying solely on small-scale NNs is ineffective for accurately approximating the Green's function near $\mathbf{x} = \mathbf{y}$ [53], since the NNs would require a large number of parameters to achieve a good approximation. Conversely, using only large-scale NN is inefficient as well, because Green's functions exhibit high smoothness, characterized by a small high-order Sobolev norm when \mathbf{x} is away from \mathbf{y} [6]. This smoothness does not necessitate large-scale networks and would lead to an unnecessary increase in the number of neurons. This is a phenomenon referred to as the low-rank matrix structure in [6]. We will further elaborate on these points later in the paper, using techniques from Barron space theory [5, 14, 37, 48, 49] to demonstrate that the proposed multiscale NN structure in (1.5) can enhance the learning efficiency by using much fewer neurons with single-scale parameters and thus significantly improve the training speed. Specifically, a large-scale NN is used to approximate the low-regularity region (cf. Theorem 1), while a small-scale NN is subsequently employed to approximate the residual of the first NN more efficiently (cf. Theorem 2). By "more efficiently", we mean that the MSNN requires fewer neurons and that the magnitude of its parameters remains moderate compared to single-scale NNs. Further details will be provided after Theorem 2.

Our main contributions of this work are summarized as follows:

- We propose a novel MSNN structure for learning Green's functions that effectively addresses the challenges of their low regularity. This approach enables the use of fewer parameters and eliminates the need for excessively large parameter magnitudes, making it more efficient than traditional single-scale NNs.

- We substantiate the advantage of using MSNN through Barron space methods, introducing the concept of the multiscale Barron space method and providing approximation error bounds for Green's functions without encountering the curse of dimensionality in the L^∞ -error with second-order derivative information. To the best of our knowledge, this is the first work to explore the multiscale Barron space and its approximation in the context of errors with second-order derivative information.
- We validate our theoretical findings and methods with numerical experiments. It is evident that, with the same number of parameters, the proposed MSNN not only learns faster but also achieves better accuracy within the same training time compared to single-scale NNs.

The remaining sections are organized as follows. In [section 2](#), we provide the necessary background and preliminaries. In [section 3](#), we introduce the proposed MSNN and prove its approximation properties. Numerical experiments are presented in [section 4](#), and we conclude in [section 5](#).

2. Preliminaries. In this section, we introduce the notations, the Rademacher complexity and the model linear PDE problem that will be used in our theoretical analysis.

2.1. Notations. The following notations will be used throughout the paper:

1. Matrices are denoted by bold uppercase letters. For example, $\mathbf{A} \in \mathbb{R}^{m \times n}$ is a real matrix of size $m \times n$ and \mathbf{A}^\top denotes the transpose of \mathbf{A} .
2. Vectors are denoted by bold lowercase letters. For example, $\mathbf{v} \in \mathbb{R}^m$ is a column vector of size m . Furthermore, we denote by $\mathbf{v}(i)$ the i -th element of \mathbf{v} .
3. Let $B_{r, \|\cdot\|_2}(\mathbf{x}) \subset \mathbb{R}^d$ be the closed ball centered at \mathbf{x} in \mathbb{R}^d with radius r measured by the Euclidean distance.

2.2. Rademacher complexity. In order to prove our main theoretical result in [Theorem 1](#), we first introduce the concept of the Rademacher complexity.

DEFINITION 1 (Rademacher complexity [\[4\]](#)). *Given a set of samples $S = \{\mathbf{z}_1, \mathbf{z}_2, \dots, \mathbf{z}_m\}$ on a domain \mathcal{Z} , and a class \mathcal{F} of real-valued functions defined on \mathcal{Z} , the empirical Rademacher complexity of \mathcal{F} in S is defined as*

$$\mathbf{R}_S(\mathcal{F}) := \frac{1}{m} \mathbb{E}_{\Xi_m} \left[\sup_{f \in \mathcal{F}} \sum_{i=1}^m \xi_i f(\mathbf{z}_i) \right],$$

where $\Xi_m := \{\xi_1, \xi_2, \dots, \xi_m\}$ is a set of m independent random samples drawn from the Rademacher distribution, i.e., $\mathbf{P}(\xi_i = +1) = \mathbf{P}(\xi_i = -1) = 1/2$, for $i = 1, 2, \dots, m$.

The following lemma bounds the expected value of the largest gap between the expected value of a function f and its empirical mean by twice the expected Rademacher complexity.

LEMMA 1 ([\[45, Lemma 26.2\]](#)). *Let \mathcal{F} be a set of functions defined on \mathcal{Z} . Then*

$$\mathbb{E}_{S \sim \rho^m} \sup_{f \in \mathcal{F}} \left(\frac{1}{m} \sum_{i=1}^m f(\mathbf{z}_i) - \mathbb{E}_{\mathbf{z} \sim \rho} f(\mathbf{z}) \right) \leq 2 \mathbb{E}_{S \sim \rho^m} \mathbf{R}_S(\mathcal{F}),$$

where $S = \{\mathbf{z}_1, \mathbf{z}_2, \dots, \mathbf{z}_m\}$ is a set of m independent random samples drawn from the distribution ρ .

2.3. The Poisson Problem. We consider the following form of the Poisson problem

$$(2.1) \quad \begin{cases} \nabla \cdot (\mathbf{A}(\mathbf{x}) \nabla u(\mathbf{x})) = g_1(\mathbf{x}), & \mathbf{x} \in \Omega \\ u(\mathbf{x}) = g_2(\mathbf{x}), & \mathbf{x} \in \partial\Omega \end{cases}$$

where $g_1(\mathbf{x})$, $g_2(\mathbf{x})$ and $u(\mathbf{x})$ are functions from \mathbb{R}^d to \mathbb{R} , $\mathbf{A}(\mathbf{x})$ is a function from \mathbb{R}^d to $\mathbb{R}^{d \times d}$, and domain $\Omega \subset [0, 1]^d$ has smooth boundaries. For any impulse source point $\mathbf{y} \in \Omega$, the Green's function of [\(2.1\)](#) satisfies the following equations:

$$(2.2) \quad \begin{cases} \nabla_{\mathbf{x}} \cdot (\mathbf{A}(\mathbf{x}) \nabla_{\mathbf{x}} G(\mathbf{x}, \mathbf{y})) = \delta(\mathbf{x} - \mathbf{y}), & \mathbf{x} \in \Omega \\ G(\mathbf{x}, \mathbf{y}) = 0, & \mathbf{x} \in \partial\Omega. \end{cases}$$

Without introducing ambiguity, we omit the notation \mathbf{x} in $\nabla_{\mathbf{x}}$ in the following discussion. The solution u of [\(2.1\)](#) can be expressed as an integral involving the Green's function, given by,

$$(2.3) \quad u(\mathbf{x}) = \int_{\Omega} g_1(\mathbf{y}) G(\mathbf{x}, \mathbf{y}) \, d\mathbf{y} - \int_{\partial\Omega} g_2(\mathbf{y}) \mathbf{A}(\mathbf{y}) (\nabla_{\mathbf{y}} G(\mathbf{x}, \mathbf{y}) \cdot \mathbf{n}_{\mathbf{y}}) \, dS(\mathbf{y}), \quad \forall \mathbf{x} \in \Omega.$$

Thus, if an approximation to the Green's function G , denoted by G_θ , that satisfies

$$(2.4) \quad \|G_\theta(\mathbf{x}, \mathbf{y}) - G(\mathbf{x}, \mathbf{y})\|_{C^1(\Omega \times \Omega)} \leq \tau \ll 1,$$

is provided, approximate solution u_θ can be effectively computed by

$$(2.5) \quad u_\theta(\mathbf{x}) := \int_{\Omega} g_1(\mathbf{y}) G_\theta(\mathbf{x}, \mathbf{y}) d\mathbf{y} - \int_{\partial\Omega} g_2(\mathbf{y}) \mathbf{A}(\mathbf{y}) (\nabla_{\mathbf{y}} G_\theta(\mathbf{x}, \mathbf{y}) \cdot \mathbf{n}_{\mathbf{y}}) dS(\mathbf{y}).$$

Furthermore, if g_1 , g_2 , and \mathbf{A} are bounded, we have

$$(2.6) \quad \|u(\mathbf{x}) - u_\theta(\mathbf{x})\|_{C^0(\Omega)} \leq C\tau,$$

where C depends only on g_1 , g_2 , and \mathbf{A} . When integral (2.5) is approximated with grid point sampling methods [24] or Monte Carlo methods [41], the approximation rate of $\mathcal{O}(M^{-\frac{1}{d}})$ or $\mathcal{O}(M^{-\frac{1}{2}})$, respectively, can be achieved, where M is the number of grid points. These results can demonstrate that learning the Green's function provides a valid approach to solving PDEs.

Building on (2.2), by approximating $\delta(\mathbf{x} - \mathbf{y})$ with the Gaussian $\mathcal{N}_\varepsilon(\mathbf{x}, \mathbf{y})$ in (1.3), we can develop an MSNN approach for an approximated G , namely G_ε , such that

$$(2.7) \quad \begin{cases} \nabla_{\mathbf{x}} \cdot (\mathbf{A}(\mathbf{x}) \nabla_{\mathbf{x}} G_\varepsilon(\mathbf{x}, \mathbf{y})) = \mathcal{N}_\varepsilon(\mathbf{x}, \mathbf{y}), & \mathbf{x} \in \Omega \\ G_\varepsilon(\mathbf{x}, \mathbf{y}) = 0, & \mathbf{x} \in \partial\Omega. \end{cases}$$

3. Multiscale Neural Networks (MSNNs). In this section, we provide details on the construction of the MSNN in (1.5). In particular, we will analyze the selection criteria for activation functions σ and σ_ε in (1.6) and prove how these choices contribute to the approximation properties of NNs.

3.1. Multiscale Barron space and activation functions. We assume that the following assumptions hold for the activation functions σ and matrix function $\mathbf{A}(\mathbf{x})$:

ASSUMPTION 1. For arbitrary $\mathbf{v} = (\mathbf{v}_x, \mathbf{v}_y) \in \mathbb{R}^{2d}$ and $\mathbf{z}_i = (\mathbf{x}_i, \mathbf{y}_i) \in [0, 1]^{2d}$ for $i = 1, 2$, let $\gamma_i = \mathbf{v} \cdot \mathbf{z}_i + b$ and $\beta = (\|\mathbf{v}\|_1 + |b|)^2$. There exists a constant $M \geq 0$ such that σ and $\mathbf{A}(\mathbf{x})$ satisfy:

$$(3.1) \quad |\sigma''(\gamma_1) \mathbf{v}_x^\top \mathbf{A}(\mathbf{x}_1) \mathbf{v}_x - \sigma''(\gamma_2) \mathbf{v}_x^\top \mathbf{A}(\mathbf{x}_2) \mathbf{v}_x| \leq \beta M |\mathbf{v} \cdot (\mathbf{z}_1 - \mathbf{z}_2)|,$$

$$(3.2) \quad |\sigma'(\gamma_1) (\nabla \cdot \mathbf{A}(\mathbf{x}_1))^\top \mathbf{v}_x - \sigma'(\gamma_2) (\nabla \cdot \mathbf{A}(\mathbf{x}_2))^\top \mathbf{v}_x| \leq \beta M |\mathbf{v} \cdot (\mathbf{z}_1 - \mathbf{z}_2)|.$$

REMARK 1. When $\mathbf{A}(\mathbf{x})$ is a constant matrix, the assumption can be directly obtained from the Lipschitz property of the activation function: $|\sigma^{(k)}(x)| \leq \sqrt{M} |x|^{3-k}$ for $k = 2, 3$, and the boundedness of \mathbf{A} , i.e., $|\mathbf{v}_x^\top \mathbf{A} \mathbf{v}_x| \leq \sqrt{M} \|\mathbf{v}_x\|_1^2$. This condition holds for most of the common activation functions, such as $\arctan(x)$ and $\tanh(x)$ used in the experiments in section 4. In the case of variable $\mathbf{A}(\mathbf{x})$, the additional requirement is that $\mathbf{A}(\mathbf{x})$ satisfies a special type of Lipschitz property, specifically in the \mathbf{v} -direction when combined with \mathbf{v}_x and σ . However, this is not the standard definition of Lipschitz continuity, so we will not delve into it further here and will simply make an assumption at this point.

Next, we describe the methodology for choosing the activation functions in terms of the parameters α and β of σ_ε in (1.6). The choice of α and β should effectively reflect the structure of the Green's function, i.e., thereby enabling NNs to approximate the Green's function accurately while minimizing the number of parameters. The optimal values of α and β depend on each other. For simplification, we set $\beta = 1$ and focus on determining the appropriate α . This approach of choosing α can be applied to other values of β . The selection of α relies on the Barron space method [5, 14, 34, 48, 49], which is a technique for approximating specific target functions using shallow NNs without suffering from the curse of dimensionality. Given the multiscale nature of the proposed approach, we adapt this technique into a multiscale Barron space method. This adaptation is necessary to evaluate errors using L^∞ -error with second-order derivative information, particularly relevant for solving second-order PDEs. To the best of our knowledge, this is the first attempt to apply the Barron space method in such a context.

When $\alpha^* \in \mathbb{R}$ and $\beta = 1$ in (1.6), the large-scale NN ϕ_1 in (1.5) can be simplified as

$$(3.3) \quad \phi_1(\mathbf{z}; \theta_1) = \frac{\varepsilon^{\alpha^*}}{n} \sum_{i=1}^n a_i \sigma(\mathbf{w}_i \cdot \mathbf{z}/\varepsilon + b_i/\varepsilon), \quad \mathbf{z} = (\mathbf{x}, \mathbf{y}), \quad \mathbf{w}_i = (\mathbf{w}_{i,x}, \mathbf{w}_{i,y}),$$

applying the linear differential operator in (2.2), it follows that

$$(3.4) \quad \nabla \cdot (\mathbf{A}(\mathbf{x}) \nabla \phi_1) = \frac{\varepsilon^{-2+\alpha^*}}{n} \sum_{i=1}^n \zeta(\mathbf{z}; a_i, \mathbf{w}_i, b_i),$$

where

$$(3.5) \quad \zeta(\mathbf{z}; a_i, \mathbf{w}_i, b_i) = a_i [\mathbf{w}_{i,\mathbf{x}}^\top \mathbf{A}(\mathbf{x}) \mathbf{w}_{i,\mathbf{x}} \sigma''(f_i) + \varepsilon (\nabla \cdot \mathbf{A}(\mathbf{x}))^\top \mathbf{w}_{i,\mathbf{x}} \sigma'(f_i)],$$

where $f_i = (\mathbf{w}_i \cdot \mathbf{z} + b_i)/\varepsilon$. This leads to the following definition of the so-called ε, α^* - $\mathbf{A}(\mathbf{x})$ -Barron function, which reduces to the classical Barron space as discussed in [14, 36] when $\varepsilon = 1$.

DEFINITION 2. [ε, α^* - $\mathbf{A}(\mathbf{x})$ -Barron function] For any $\varepsilon \in (0, 1]$ and $\alpha^* \in \mathbb{R}$, function $f(\mathbf{x}, \mathbf{y}) : \Omega \times \Omega \rightarrow \mathbb{R}$ is called an ε, α^* - $\mathbf{A}(\mathbf{x})$ -Barron function with respect to $\sigma(x)$, if there exists a probability distribution ρ over \mathbb{R}^{d+2} such that

$$(3.6) \quad f(\mathbf{x}, \mathbf{y}) = \mathbb{E}_{(a, \mathbf{w}, b) \sim \rho} \varepsilon^{-2+\alpha^*} \zeta(\mathbf{z}; a, \mathbf{w}, b).$$

For ε, α^* - $\mathbf{A}(\mathbf{x})$ -Barron functions, we can define the Barron-norm constant.

DEFINITION 3. Suppose that the function $f(\mathbf{x}, \mathbf{y}) : \Omega \times \Omega \rightarrow \mathbb{R}$ is an ε, α^* - $\mathbf{A}(\mathbf{x})$ -Barron function with respect to $\sigma(x)$. The Barron-norm constant of f is defined as

$$(3.7) \quad \|f\|_{\mathcal{B}_{\varepsilon, \alpha^*}} := \inf_{\rho \in \mathcal{P}} \sqrt{\mathbb{E}_{(a, \mathbf{w}, b) \sim \rho} (|a| (\|\mathbf{w}\|_1^3 + 2\|\mathbf{w}\|_1^2 |b| + \|\mathbf{w}\|_1 |b|^2))}$$

where \mathcal{P} is the set of all probability distributions ρ over \mathbb{R}^{d+2} that satisfy the condition (3.6).

This definition is consistent with that in [37, 38] when $p = 2$ in their context and match the definition in [36] when (\mathbf{w}, b) is replaced by $\bar{\mathbf{w}}$. In [37, 38], the authors use the definition of the Barron norm for $p = \infty$ because the space is sufficiently large when the activation functions are ReLU due to the homogeneity of ReLU, which ensures that the spaces for $1 \leq p \leq \infty$ are equivalent. However, since our work does not restrict to ReLU activation function, the proof differs, and we perform it specially for the $p = 2$ case.

The difference between our definition of Barron-type space and others is that we introduce a smaller term ε in the definition, which we call the *multiscale Barron space method*. The following definitions are also based on the multiscale Barron space method. We first establish a large-scale NN to approximate the Green's function, in Theorem 1, based on the large-scale Barron space, i.e., ε, α^* - $\mathbf{A}(\mathbf{x})$ -Barron function for $\varepsilon \ll 1$. Then, we establish a small-scale NN based on the small-scale Barron space, i.e., $\varepsilon = 1$, in Definition 2, to approximate the residual from the first step.

LEMMA 2. For $\alpha_1^*, \alpha_2^* \in \mathbb{R}$ and $\varepsilon \in (0, 1]$, if function f is an ε, α_1^* - $\mathbf{A}(\mathbf{x})$ -Barron function, then it is also an ε, α_2^* - $\mathbf{A}(\mathbf{x})$ -Barron function. Furthermore, we have

$$(3.8) \quad \frac{\|f\|_{\mathcal{B}_{\varepsilon, \alpha_1^*}}}{\|f\|_{\mathcal{B}_{\varepsilon, \alpha_2^*}}} = \varepsilon^{-\alpha_1^* + \alpha_2^*}.$$

Proof. For f to be an ε, α_1^* - $\mathbf{A}(\mathbf{x})$ -Barron function, it means that we can find a probability distribution ρ_1 such that

$$(3.9) \quad f(\mathbf{x}, \mathbf{y}) = \mathbb{E}_{(a, \mathbf{w}, b) \sim \rho_1} \varepsilon^{-2+\alpha_1^*} a [\mathbf{w}_x^\top \mathbf{A}(\mathbf{x}) \mathbf{w}_x \sigma''(d) + \varepsilon (\nabla \cdot \mathbf{A}(\mathbf{x}))^\top \mathbf{w}_x \sigma'(d)],$$

where $d = (\mathbf{w} \cdot \mathbf{z} + b)/\varepsilon$. With simple calculation, we have

$$(3.10) \quad f(\mathbf{x}, \mathbf{y}) = \mathbb{E}_{(a, \mathbf{w}, b) \sim \rho_1} \varepsilon^{-2+\alpha_2^*} \varepsilon^{\alpha_1^* - \alpha_2^*} a [\mathbf{w}_x^\top \mathbf{A}(\mathbf{x}) \mathbf{w}_x \varepsilon_1 \sigma''(d) + \varepsilon (\nabla \cdot \mathbf{A}(\mathbf{x}))^\top \mathbf{w}_x \sigma'(d)].$$

Then set $\hat{a} = \varepsilon^{\alpha_1^* - \alpha_2^*} a$, we can show that there exists a distribution ρ_2 such that

$$(3.11) \quad f(\mathbf{x}, \mathbf{y}) = \mathbb{E}_{(\hat{a}, \mathbf{w}, b) \sim \rho_2} \varepsilon^{-2+\alpha_2^*} \hat{a} [\mathbf{w}_x^\top \mathbf{A}(\mathbf{x}) \mathbf{w}_x \sigma''(d) + \varepsilon (\nabla \cdot \mathbf{A}(\mathbf{x}))^\top \mathbf{w}_x \sigma'(d)],$$

where ρ_2 is just a rescaling of ρ_1 . Furthermore, we have

$$(3.12) \quad \mathbb{E}_{(a, \mathbf{w}, b) \sim \rho_1} (\eta |a|)^2 = \varepsilon^{-2(\alpha_1^* - \alpha_2^*)} \mathbb{E}_{(\hat{a}, \mathbf{w}, b) \sim \rho_2} (\eta |\hat{a}|)^2, \quad \eta = \|\mathbf{w}\|_1^3 + 2\|\mathbf{w}\|_1^2 |b| + \|\mathbf{w}\|_1 |b|^2.$$

The above still holds for the $\inf_{\rho \in \mathcal{P}}$ calculation since they are proportional, therefore (3.8) follows. \square

REMARK 2. *Lemma 2* tells us two facts: First, in a multiscale Barron space method, for a fixed ε , whether a function is an ε, α^* - $\mathbf{A}(\mathbf{x})$ -Barron function or not does not depend on α^* , although the magnitude of the Barron-norm constant does. This shows that allowing a function to belong to an ε, α^* - $\mathbf{A}(\mathbf{x})$ -Barron function for all α^* for a fixed ε is not an overly restrictive assumption. In the following sections, we will perform the theoretical analysis based on the assumption that for a fixed ε , $\mathcal{N}_\varepsilon(\mathbf{x}, \mathbf{y})$ is an ε, α^* - $\mathbf{A}(\mathbf{x})$ -Barron function for all α^* . Given the high smoothness of $\mathcal{N}_\varepsilon(\mathbf{x}, \mathbf{y})$, this assumption should hold in most cases based on [56, Theorem 3.1]. If not, we can still establish the approximation theory using Sobolev approximation [46, 62], which, despite the curse of dimensionality, retains the advantage of the MSNN. Second, for a fixed $\varepsilon \in (0, 1)$, a larger α^* results in a larger Barron-norm constant. When $\varepsilon = 1$, the constants are the same, thus we denote by $\|f\|_{\mathcal{B}_1}$ the Barron-norm constant and refer to $1, \alpha^*$ - $\mathbf{A}(\mathbf{x})$ -Barron functions as 1 - $\mathbf{A}(\mathbf{x})$ -Barron functions for simplicity.

3.2. Approximation property of MSNN. Provided that *Assumption 1* holds, we can show the approximation rate of the proposed MSNN in the next two theorems. The difficulties in our approximation arise because we are approximating the Green's function based on the PDE (2.2), which requires the approximation to contain derivative information for both the NNs and the Green's function. Classical L^2 or L^∞ -approximations, which do not contain derivative information, such as those in [37], are not sufficient. Furthermore, when approximating Green's functions, the most challenging part is the region near $\mathbf{x} = \mathbf{y}$. If we consider H^2 approximation, we cannot ensure that this region is approximated well when the overall error is small, because the measure of that region is small compared to the whole domain. Therefore, we need to consider the L^∞ -error with second-order derivative information in the approximation.

THEOREM 1. *For any $\varepsilon \in (0, 1]$, suppose $\mathcal{N}_\varepsilon(\mathbf{x}, \mathbf{y}) : \Omega \times \Omega \rightarrow \mathbb{R}$ is an ε, α^* - $\mathbf{A}(\mathbf{x})$ -Barron function with respect to $\sigma(x)$ for all $\alpha^* \in \mathbb{R}$, and *Assumption 1* holds and $\mathbf{z} = (\mathbf{x}, \mathbf{y})$. Then for any $n \geq 1$, there exists a set of large-scale NNs, denoted by \mathcal{A}_n , with activation function σ_ε in (1.6), a finite α^* associated with $\beta = 1$, i.e.,*

$$(3.13) \quad \mathcal{A}_n \subset \left\{ \phi_1 \mid \phi_1(\mathbf{z}; \boldsymbol{\theta}) = \frac{1}{n} \sum_{i=1}^n a_i \sigma_\varepsilon(\mathbf{w}_i \cdot \mathbf{z} + b_i) \right\}$$

such that for any $\phi_1(\mathbf{z}; \boldsymbol{\theta}) \in \mathcal{A}_n$, we have

$$(3.14) \quad \sup_{\mathbf{x}, \mathbf{y}} |\nabla \cdot (\mathbf{A}(\mathbf{x}) \nabla \phi_1(\mathbf{z}; \boldsymbol{\theta})) - \mathcal{N}_\varepsilon(\mathbf{x}, \mathbf{y})| \leq \frac{8M\sqrt{2d}\|\mathcal{N}_\varepsilon\|_{\mathcal{B}_{\varepsilon, \alpha^*}}}{\varepsilon^{-\alpha^*+3}\sqrt{n}}$$

and

$$(3.15) \quad \frac{1}{n} \sum_{i=1}^n (|a_i| (\|\mathbf{w}_i\|_1^3 + 2\|\mathbf{w}_i\|_1^2 |b_i| + \|\mathbf{w}_i\|_1 |b_i|^2))^2 \leq 3\|\mathcal{N}_\varepsilon\|_{\mathcal{B}_{\varepsilon, \alpha^*}}^2$$

where M is the constant defined in *Assumption 1*.

Proof. By the definitions of ε, α^* - $\mathbf{A}(\mathbf{x})$ -Barron function, there exists a probability density ρ such that

$$(3.16) \quad \mathcal{N}_\varepsilon(\mathbf{x}, \mathbf{y}) = \mathbb{E}_{(a, \mathbf{w}, b) \sim \rho} \varepsilon^{-2+\alpha^*} \zeta(\mathbf{z}; a, \mathbf{w}, b),$$

for all $\mathbf{z} = (\mathbf{x}, \mathbf{y}) \in \Omega \times \Omega$, where ζ is defined in (3.5), and

$$(3.17) \quad \sqrt{\mathbb{E}_{(a, \mathbf{w}, b) \sim \rho} [a^2 (\|\mathbf{w}\|_1^3 + 2\|\mathbf{w}\|_1^2 |b| + \|\mathbf{w}\|_1 |b|^2)]^2} \leq (1 + \delta) \|\mathcal{N}_\varepsilon\|_{\mathcal{B}_{\varepsilon, \alpha^*}} < \frac{9}{8} \|\mathcal{N}_\varepsilon\|_{\mathcal{B}_{\varepsilon, \alpha^*}},$$

where δ is a small constant larger than 0. We need to prove there exists $\{\zeta_i\}_{i=1}^n$ such that

$$(3.18) \quad \sup_{\mathbf{z}} \left| \frac{1}{n} \sum_{i=1}^n (\varepsilon^{-2+\alpha^*} \zeta_i - \mathcal{N}_\varepsilon) \right| \leq \frac{8M\sqrt{2d}\|\mathcal{N}_\varepsilon\|_{\mathcal{B}_{\varepsilon, \alpha^*}}}{\varepsilon^{-\alpha^*+3}\sqrt{n}}, \quad \zeta_i \equiv \zeta(\mathbf{z}; a_i, \mathbf{w}_i, b_i).$$

The idea of the proof is to choose $\{\zeta_i\}_{i=1}^n$ with i.i.d. probability distribution $(a_i, \mathbf{w}_i, b_i)_{i=1}^n \sim \rho^n$ for $i = 1, \dots, n$, and then bound the expectation of $\frac{1}{n} \sum_{i=1}^n (\varepsilon^{-2+\alpha^*} \zeta_i - \mathcal{N}_\varepsilon)$. This allows us to show that there exists a sample satisfying the error bound established earlier.

From [Lemma 1](#), we have

$$(3.19) \quad \mathbb{E}_{(a_i, \mathbf{w}_i, b_i)_{i=1}^n \sim \rho^n} \left[\sup_{\mathbf{z}} \frac{1}{n} \sum_{i=1}^n \left(\varepsilon^{-2+\alpha^*} \zeta_i - \mathcal{N}_\varepsilon \right) \right] \leq \frac{2}{\varepsilon^{2-\alpha^*}} \mathbb{E}_{(a_i, \mathbf{w}_i, b_i)_{i=1}^n \sim \rho^n} \mathbb{E}_{\Xi_n} \left[\sup_{\mathbf{z}} \frac{1}{n} \sum_{i=1}^n \xi_i \zeta_i \right]$$

where $\Xi_n = \{\xi_1, \xi_2, \dots, \xi_n\}$ are independent random samples drawn from the Rademacher distribution, i.e., $\mathbf{P}(\xi_i = +1) = \mathbf{P}(\xi_i = -1) = 1/2$, for $i = 1, 2, \dots, n$. The inequality (3.19) is by the definition of the Rademacher complexities in [Definition 1](#).

We next estimate the last term of (3.19), i.e.,

$$(3.20) \quad \mathbb{E}_{\Xi_n} \left[\sup_{\mathbf{z}} \frac{1}{n} \sum \xi_i \zeta_i \right] \leq \mathbb{E}_{\Xi_n} \left[\sup_{\mathbf{z}} \frac{1}{n} \sum a_i \xi_i \mathbf{w}_{i,x}^\top \mathbf{A}(\mathbf{x}) \mathbf{w}_{i,x} \sigma''(f_i(\mathbf{z})) \right] +$$

$$(3.21) \quad \mathbb{E}_{\Xi_n} \left[\sup_{\mathbf{z}} \frac{1}{n} \sum a_i \xi_i \varepsilon (\nabla \cdot \mathbf{A}(\mathbf{x}))^\top \mathbf{w}_i \sigma'(f_i(\mathbf{z})) \right],$$

where $f_i(\mathbf{z}) = (\mathbf{w}_i \cdot \mathbf{z} + b_i)/\varepsilon$. For the first term of the right-hand side of the above inequality, we have

$$(3.22) \quad \begin{aligned} & \mathbb{E}_{\Xi_n} \left[\sup_{\mathbf{z}} \frac{1}{n} \sum \xi_i a_i \mathbf{w}_{i,x}^\top \mathbf{A}(\mathbf{x}) \mathbf{w}_{i,x} \sigma''(f_i(\mathbf{z})) \right] \\ &= \frac{1}{2n} \mathbb{E}_{\xi_2, \dots, \xi_m} \left[\sup_{\mathbf{z}} \left(a_1 \mathbf{w}_{1,x}^\top \mathbf{A}(\mathbf{x}) \mathbf{w}_{1,x} \sigma''(f_1(\mathbf{z})) + \sum_{i=2}^m \xi_i a_i \mathbf{w}_{i,x}^\top \mathbf{A}(\mathbf{x}) \mathbf{w}_{i,x} \sigma''(f_i(\mathbf{z})) \right) \right. \\ & \quad \left. + \sup_{\mathbf{z}} \left(-a_1 \mathbf{w}_{1,x}^\top \mathbf{A}(\mathbf{x}) \mathbf{w}_{1,x} \sigma''(f_1(\mathbf{z})) + \sum_{i=2}^m \xi_i a_i \mathbf{w}_{i,x}^\top \mathbf{A}(\mathbf{x}) \mathbf{w}_{i,x} \sigma''(f_i(\mathbf{z})) \right) \right] \\ &= \frac{1}{2n} \mathbb{E}_{\xi_2, \dots, \xi_m} \left[\sup_{\mathbf{z}_1, \mathbf{z}_2} \left(a_1 \mathbf{w}_{1,x}^\top \mathbf{A}(\mathbf{x}_1) \mathbf{w}_{1,x} \sigma''(f_1(\mathbf{z}_1)) - a_1 \mathbf{w}_{1,x}^\top \mathbf{A}(\mathbf{x}_2) \mathbf{w}_{1,x} \sigma''(f_1(\mathbf{z}_2)) \right) \right. \\ & \quad \left. + \sum_{i=2}^m \xi_i a_i \mathbf{w}_{i,x}^\top \mathbf{A}(\mathbf{x}_1) \mathbf{w}_{i,x} \sigma''(f_i(\mathbf{z}_1)) + \sum_{i=2}^m \xi_i a_i \mathbf{w}_{i,x}^\top \mathbf{A}(\mathbf{x}_2) \mathbf{w}_{i,x} \sigma''(f_i(\mathbf{z}_2)) \right]. \end{aligned}$$

By [Assumption 1](#) we have inequality

$$(3.23) \quad \begin{aligned} & a_1 \mathbf{w}_{1,x}^\top \mathbf{A}(\mathbf{x}_1) \mathbf{w}_{1,x} \sigma''(f_1(\mathbf{z}_1)) - a_1 \mathbf{w}_{1,x}^\top \mathbf{A}(\mathbf{x}_2) \mathbf{w}_{1,x} \sigma''(f_1(\mathbf{z}_2)) \\ &= a_1 \varepsilon^2 \frac{\mathbf{w}_{1,x}^\top}{\varepsilon} \mathbf{A}(\mathbf{x}_1) \frac{\mathbf{w}_{1,x}}{\varepsilon} \sigma''((\mathbf{w}_1 \cdot \mathbf{z}_1 + b_1)/\varepsilon) - a_1 \varepsilon^2 \frac{\mathbf{w}_{1,x}^\top}{\varepsilon} \mathbf{A}(\mathbf{x}_2) \frac{\mathbf{w}_{1,x}}{\varepsilon} \sigma''((\mathbf{w}_1 \cdot \mathbf{z}_2 + b_1)/\varepsilon) \\ &\leq M |a_1| (\|\mathbf{w}_1\|_1 + |b_1|)^2 \left(\frac{1}{\varepsilon} |\mathbf{w}_1 \cdot (\mathbf{z}_1 - \mathbf{z}_2)| \right). \end{aligned}$$

Substituting (3.23) into (3.22), we obtain

$$\begin{aligned} & \mathbb{E}_{\Xi_n} \left[\sup_{\mathbf{z}} \frac{1}{n} \sum \xi_i a_i \mathbf{w}_{i,x}^\top \mathbf{A}(\mathbf{x}) \mathbf{w}_{i,x} \sigma''(f_i) \right] \\ &\leq \frac{1}{2n} \mathbb{E}_{\xi_2, \dots, \xi_m} \left[\sup_{\mathbf{z}_1, \mathbf{z}_2} \left(\frac{M}{\varepsilon} |a_1| (\|\mathbf{w}_1\|_1 + |b_1|)^2 |\mathbf{w}_1 \cdot (\mathbf{z}_1 - \mathbf{z}_2)| \right. \right. \\ & \quad \left. \left. + \sum_{i=2}^m \xi_i a_i \mathbf{w}_{i,x}^\top \mathbf{A}(\mathbf{x}_1) \mathbf{w}_{i,x} \sigma''(f_i(\mathbf{z}_1)) + \sum_{i=2}^m \xi_i a_i \mathbf{w}_{i,x}^\top \mathbf{A}(\mathbf{x}_2) \mathbf{w}_{i,x} \sigma''(f_i(\mathbf{z}_2)) \right) \right] \\ &= \frac{1}{2n} \mathbb{E}_{\xi_2, \dots, \xi_m} \left[\sup_{\mathbf{z}_1, \mathbf{z}_2} \left(\frac{M}{\varepsilon} |a_1| (\|\mathbf{w}_1\|_1 + |b_1|)^2 (\mathbf{w}_1 \cdot \mathbf{z}_1 - \mathbf{w}_1 \cdot \mathbf{z}_2) \right. \right. \\ & \quad \left. \left. + \sum_{i=2}^m \xi_i a_i \mathbf{w}_{i,x}^\top \mathbf{A}(\mathbf{x}_1) \mathbf{w}_{i,x} \sigma''(f_i(\mathbf{z}_1)) + \sum_{i=2}^m \xi_i a_i \mathbf{w}_{i,x}^\top \mathbf{A}(\mathbf{x}_2) \mathbf{w}_{i,x} \sigma''(f_i(\mathbf{z}_2)) \right) \right] \\ &= \mathbb{E}_{\Xi_n} \left[\sup_{\mathbf{z}} \frac{1}{n} \left(\varepsilon^{-1} |a_1| M (\|\mathbf{w}_1\|_1 + |b_1|)^2 \xi_1 \mathbf{w}_1 \cdot \mathbf{z} + \sum_{i=2}^m \xi_i a_i \mathbf{w}_{i,x}^\top \mathbf{A}(\mathbf{x}) \mathbf{w}_{i,x} \sigma''(f_i(\mathbf{z})) \right) \right], \end{aligned}$$

Repeating this process n times, we have

$$(3.24) \quad \mathbb{E}_{\Xi_n} \left[\sup_{\mathbf{z}} \frac{1}{n} \sum \xi_i a_i \mathbf{w}_{i,\mathbf{x}}^\top \mathbf{A}(\mathbf{x}) \mathbf{w}_{i,\mathbf{x}} \sigma''(f_i) \right]$$

$$(3.25) \quad \leq \mathbb{E}_{\Xi_n} \left[\sup_{\mathbf{z}} \frac{1}{n} \sum_{i=1}^m \varepsilon^{-1} |a_i| M (\|\mathbf{w}_i\|_1 + |b_i|)^2 \xi_i \mathbf{w}_i \cdot \mathbf{z} \right]$$

$$(3.26) \quad \leq \varepsilon^{-1} M \mathbb{E}_{\Xi_n} \left\| \frac{1}{n} \sum_{i=1}^m \xi_i |a_i| (\|\mathbf{w}_i\|_1 + |b_i|)^2 \mathbf{w}_i \right\|_1.$$

Similarly, we have

$$(3.27) \quad \mathbb{E}_{\Xi_n} \left[\sup_{\mathbf{z}} \frac{1}{n} \sum a_i \xi_i \varepsilon (\nabla \cdot \mathbf{A}(\mathbf{x}))^\top \mathbf{w}_i \sigma'(f_i) \right] \leq \varepsilon^{-1} M \mathbb{E}_{\Xi_n} \left\| \frac{1}{n} \sum_{i=1}^m \xi_i |a_i| (\|\mathbf{w}_i\|_1 + |b_i|)^2 \mathbf{w}_i \right\|_1.$$

It follows from (3.17) that the expectations of the following term in the summations of (3.26) and (3.27) are less than $(1 + \delta) \|\mathcal{N}_\varepsilon\|_{\mathcal{B}_{\varepsilon,\alpha^*}}$, i.e.,

$$(3.28) \quad \sqrt{\mathbb{E}_{(a_i, \mathbf{w}_i, b_i) \sim \rho} \|\mathbf{q}_i\|_1^2} \leq (1 + \delta) \|\mathcal{N}_\varepsilon\|_{\mathcal{B}_{\varepsilon,\alpha^*}}, \quad \mathbf{q}_i \equiv |a_i| (\|\mathbf{w}_i\|_1 + |b_i|)^2 \mathbf{w}_i.$$

Putting together, we have

$$(3.29) \quad \mathbb{E}_{(a_i, \mathbf{w}_i, b_i)_{i=1}^n \sim \rho^n} \left[\sup_{\mathbf{z}} \frac{1}{n} \sum \left(\varepsilon^{-2-\alpha^*} \zeta_i - \mathcal{N}_\varepsilon \right) \right]$$

$$(3.30) \quad \leq \mathbb{E}_{(a_i, \mathbf{w}_i, b_i)_{i=1}^n \sim \rho^n} \frac{4M}{\varepsilon^{3-\alpha^*}} \mathbb{E}_{\Xi_n} \left\| \frac{1}{n} \sum \xi_i \mathbf{q}_i \right\|_1$$

$$(3.31) \quad \leq \frac{4M\sqrt{2d}}{\varepsilon^{3-\alpha^*}} \mathbb{E}_{(a_i, \mathbf{w}_i, b_i)_{i=1}^n \sim \rho^n} \mathbb{E}_{\Xi_n} \left\| \frac{1}{n} \sum \xi_i \mathbf{q}_i \right\|_2$$

$$(3.32) \quad \leq \frac{4M\sqrt{2d}}{n\varepsilon^{3-\alpha^*}} \sqrt{\mathbb{E}_{(a_i, \mathbf{w}_i, b_i)_{i=1}^n \sim \rho^n} \mathbb{E}_{\Xi_n} \left\| \sum \xi_i \mathbf{q}_i \right\|_2^2},$$

where $\|\mathbf{z}\|_2 \leq \|\mathbf{z}\|_1 \leq \sqrt{2d}\|\mathbf{z}\|_2$, $\forall \mathbf{z} \in \mathbb{R}^{2d}$ is used, and the last step is due to Jensen's inequality. By the direct calculation, we know the cross-terms will disappear under the expectation, therefore, we have

$$(3.33) \quad \mathbb{E}_{(a_i, \mathbf{w}_i, b_i)_{i=1}^n \sim \rho^n} \left[\sup_{\mathbf{z}} \frac{1}{n} \sum \left(\varepsilon^{-2-\alpha^*} \zeta_i - \mathcal{N}_\varepsilon \right) \right]$$

$$(3.34) \quad \leq \frac{4M\sqrt{2d}}{n\varepsilon^{3-\alpha^*}} \sqrt{\mathbb{E}_{(a_i, \mathbf{w}_i, b_i)_{i=1}^n \sim \rho^n} \sum \|\mathbf{q}_i\|_2^2}$$

$$(3.35) \quad \leq \frac{4M\sqrt{2d}}{n\varepsilon^{3-\alpha^*}} \sqrt{\mathbb{E}_{(a_i, \mathbf{w}_i, b_i)_{i=1}^n \sim \rho^n} \sum \|\mathbf{q}_i\|_1^2}$$

$$(3.36) \quad \leq \frac{4(1 + \delta)M\sqrt{2d}\|\mathcal{N}_\varepsilon\|_{\mathcal{B}_{\varepsilon,\alpha^*}}}{\varepsilon^{3-\alpha^*}\sqrt{n}}.$$

Similarly, we can show

$$(3.37) \quad \mathbb{E}_{(a_i, \mathbf{w}_i, b_i)_{i=1}^n \sim \rho^n} \left[-\sup_{\mathbf{z}} \frac{1}{n} \sum \left(\varepsilon^{-2+\alpha^*} \zeta_i - \mathcal{N}_\varepsilon \right) \right] \leq \frac{4(1 + \delta)M\sqrt{2d}\|\mathcal{N}_\varepsilon\|_{\mathcal{B}_{\varepsilon,\alpha^*}}}{\varepsilon^{3-\alpha^*}\sqrt{n}},$$

from which and (3.36), we finally can show that

$$(3.38) \quad \mathbb{E}_{(a_i, \mathbf{w}_i, b_i)_{i=1}^n \sim \rho^n} \sup_{\mathbf{z}} \left| \frac{1}{n} \sum \left(\varepsilon^{-2+\alpha^*} \zeta_i - \mathcal{N}_\varepsilon \right) \right| \leq \frac{4(1 + \delta)M\sqrt{2d}\|\mathcal{N}_\varepsilon\|_{\mathcal{B}_{\varepsilon,\alpha^*}}}{\varepsilon^{3-\alpha^*}\sqrt{n}},$$

and furthermore

$$(3.39) \quad \mathbb{E}_{(a_i, \mathbf{w}_i, b_i)_{i=1}^n \sim \rho^n} \frac{1}{n} \sum \left(|a_i| (\|\mathbf{w}_i\|_1^3 + 2\|\mathbf{w}_i\|_1^2 |b_i| + \|\mathbf{w}_i\|_1 |b_i|^2) \right)^2 \leq (1 + \delta)^2 \|\mathcal{N}_\varepsilon\|_{\mathcal{B}_{\varepsilon,\alpha^*}}^2.$$

Denote by \mathcal{E}_1 and \mathcal{E}_2 the two terms in the expectations, i.e.,

$$(3.40) \quad \mathcal{E}_1(\{a_i, \mathbf{w}_i, b_i\}) = \sup_{\mathbf{z}} \left| \frac{1}{n} \sum \left(\varepsilon^{-2+\alpha^*} \zeta_i - \mathcal{N}_\varepsilon \right) \right|$$

$$(3.41) \quad \mathcal{E}_2(\{a_i, \mathbf{w}_i, b_i\}) = \frac{1}{n} \sum (|a_i| (\|\mathbf{w}_i\|_1^3 + 2\|\mathbf{w}_i\|_1^2 |b_i| + \|\mathbf{w}_i\|_1 |b_i|^2))^2,$$

and define two events

$$(3.42) \quad E_1 = \left\{ \mathcal{E}_1 < \frac{8M\sqrt{2d}\|\mathcal{N}_\varepsilon\|_{\mathcal{B}_{\varepsilon,\alpha^*}}}{\varepsilon^{3-\alpha^*}\sqrt{n}} \right\}, \quad E_2 = \left\{ \mathcal{E}_2 < 3\|\mathcal{N}_\varepsilon\|_{\mathcal{B}_{\varepsilon,\alpha^*}}^2 \right\}.$$

Based on Markov's inequality, we have

$$(3.43) \quad \begin{aligned} \mathbf{P}(E_1) &\geq 1 - \frac{\mathbb{E}(\mathcal{E}_1)}{\frac{8M\sqrt{2d}\|\mathcal{N}_\varepsilon\|_{\mathcal{B}_{\varepsilon,\alpha^*}}}{\varepsilon^{3-\alpha^*}\sqrt{n}}} > \frac{7}{16}, \\ \mathbf{P}(E_2) &\geq 1 - \frac{\mathbb{E}(\mathcal{E}_2)}{3\|\mathcal{N}_\varepsilon\|_{\mathcal{B}_{\varepsilon,\alpha^*}}^2} > \frac{37}{64}, \end{aligned}$$

so that $\mathbf{P}(E_1 \cap E_2) > \frac{1}{64}$, indicating that there exist $(a_i, \mathbf{w}_i, b_i)_{i=1}^n$ such that (3.14) and (3.15) are true. We can collect all such weights and construct the NNs in \mathcal{A}_n . \square

Based on Theorem 1, we know that when α^* satisfies $\|\mathcal{N}_\varepsilon(\mathbf{x}, \mathbf{y})\|_{\mathcal{B}_{\varepsilon,\alpha^*}} \leq 1$, it ensures that the average magnitude of the parameters is not large. However, we also do not want to choose a too small α^* , as that might result in a larger n reaching the same approximation accuracy due to the increase in the denominator in the upper bound of (3.14). Therefore, we suggest choosing an α^* such that $\|\mathcal{N}_\varepsilon(\mathbf{x}, \mathbf{y})\|_{\mathcal{B}_{\varepsilon,\alpha^*}} \approx 1$. Based on Lemma 2, we know that for a fixed ε , a larger α^* results in a larger Barron norm. Therefore, we can pick the following α :

$$(3.44) \quad \alpha = \sup \{ \alpha^* \mid \|\mathcal{N}_\varepsilon(\mathbf{x}, \mathbf{y})\|_{\mathcal{B}_{\varepsilon,\alpha^*}} \leq 1 \}.$$

Based on Lemma 2, for any fixed $\varepsilon > 0$, there are either infinite elements or none in

$$\{ \alpha^* \mid \|\mathcal{N}_\varepsilon(\mathbf{x}, \mathbf{y})\|_{\mathcal{B}_{\varepsilon,\alpha^*}} \leq 1 \}.$$

If $\{ \alpha^* \mid \|\mathcal{N}_\varepsilon(\mathbf{x}, \mathbf{y})\|_{\mathcal{B}_{\varepsilon,\alpha^*}} \leq 1 \} = \emptyset$, we define $\alpha = -\infty$. This indicates that no large-scale NNs can even roughly approximate the Green's function of (2.1) for $\beta = 1$. This issue arises from the excessive complexity of $\mathbf{A}(\mathbf{x})$ and Ω , scenarios which will not be addressed in this paper. If there are infinite elements in that set, there must be an upper bound based on Lemma 2; therefore, α cannot be $+\infty$. By choosing such α , we can ensure that the number of the parameters n in the large-scale network can be small.

Theorem 1 provides the approximation property of the large-scale NN. Next, we analyze the approximation property of the MSNN. Before proceeding to Theorem 2, we discuss an assumption in Theorem 2 in more detail. In the theorem, we assume that

$$r_n(\mathbf{x}, \mathbf{y}) = \nabla \cdot (\mathbf{A}(\mathbf{x}) \nabla \phi_1(\mathbf{z}; \boldsymbol{\theta}_1)) - \mathcal{N}_\varepsilon(\mathbf{x}, \mathbf{y})$$

is a 1- $\mathbf{A}(\mathbf{x})$ -Barron function with respect to $\sigma(x)$. This assumption is reasonable due to [56], which shows that sufficiently smooth functions belong to Barron-type spaces. Here, for any $\varepsilon > 0$, \mathcal{N}_ε is smooth and $\nabla \cdot (\mathbf{A}(\mathbf{x}) \nabla \phi_1(\mathbf{z}; \boldsymbol{\theta}_1))$ is also smooth if \mathbf{A} and σ are smooth. Without being rigorous, we treat this as an assumption.

THEOREM 2. *Under the same assumptions in Theorem 1, if there is a large-scale NN, denoted by $\phi_1(\mathbf{z}; \boldsymbol{\theta}_1) \in \mathcal{A}_n$, such that*

$$r_n(\mathbf{x}, \mathbf{y}) = \nabla \cdot (\mathbf{A}(\mathbf{x}) \nabla \phi_1(\mathbf{z}; \boldsymbol{\theta}_1)) - \mathcal{N}_\varepsilon(\mathbf{x}, \mathbf{y})$$

is a 1- $\mathbf{A}(\mathbf{x})$ -Barron function with respect to $\sigma(x)$, for any $m \geq 1$, there exists a small-scale NN with activation function $\sigma(x)$,

$$\phi_2(\mathbf{z}; \boldsymbol{\theta}_2) = \sum_{i=n+1}^{m+n} \frac{1}{m} a_i \sigma(\mathbf{w}_i \cdot \mathbf{z} + b_i)$$

such that for $\phi(\mathbf{z}, \boldsymbol{\theta}) = \phi_1(\mathbf{z}, \boldsymbol{\theta}_1) + \phi_2(\mathbf{z}, \boldsymbol{\theta}_2)$ in (1.5), we have

$$(3.45) \quad \sup_{\mathbf{x}, \mathbf{y}} |\nabla \cdot (\mathbf{A}(\mathbf{x}) \nabla \phi(\mathbf{z}; \boldsymbol{\theta})) - \mathcal{N}_\varepsilon(\mathbf{x}, \mathbf{y})| \leq \|r_n(\mathbf{x}, \mathbf{y})\|_{\mathcal{B}_1} \frac{8M\sqrt{2d}}{\sqrt{m}}$$

and

$$(3.46) \quad \frac{1}{m} \sum_{i=n+1}^{n+m} (|a_i| (\|\mathbf{w}_i\|_1^3 + 2\|\mathbf{w}_i\|_1^2 |b_i| + \|\mathbf{w}_i\|_1 |b_i|^2))^2 \leq 3\|r_n(\mathbf{x}, \mathbf{y})\|_{\mathcal{B}_1}^2.$$

Proof. The proof is similar to that of Theorem 1, and is therefore omitted here. \square

Theorems 1 and 2 provide the approximation properties of the MSNN and illustrate the advantages of employing the MSNN in (1.5) over single-scale NNs. If only a large-scale NN $\phi_1(\mathbf{z}; \boldsymbol{\theta}_1)$ is used to approximate the Green's function, $\mathcal{O}((\varepsilon^{-\alpha^*+3}\hat{\varepsilon})^{-2})$ parameters are required to achieve an error of $\mathcal{O}(\hat{\varepsilon})$ according to (3.14). If we only have a small-scale NN, i.e., $\phi_1 = 0$ in Theorem 2, the magnitude of the parameters will be large due to (3.46) and the fact that $\|\mathcal{N}_\varepsilon\|_{\mathcal{B}_1}$ is large. On the other hand, by adopting the MSNN approach, it is possible to use only $\mathcal{O}(\varepsilon^{2(\alpha^*-3)} + \hat{\varepsilon}^{-2})$ parameters to achieve an error of $\mathcal{O}(\hat{\varepsilon})$. The reason is that when using MSNN with $m \geq 1$ and under the assumption that $\sup_{\mathbf{x}, \mathbf{y}} |r_n(\mathbf{x}, \mathbf{y})| = \mathcal{O}(1)$, we can possibly have the estimate $\|r_n(\mathbf{x}, \mathbf{y})\|_{\mathcal{B}_1} = \mathcal{O}(1)$. Then the upper bound in (3.45) can be simplified as

$$(3.47) \quad \sup_{\mathbf{z}} |\nabla \cdot (\mathbf{A}(\mathbf{x}) \nabla \phi(\mathbf{z}; \boldsymbol{\theta})) - \mathcal{N}_\varepsilon(\mathbf{x}, \mathbf{y})| \leq \frac{C_2}{\sqrt{m}},$$

where C_2 is $\mathcal{O}(1)$ respect to ε .

For $\|r_n(\mathbf{x}, \mathbf{y})\|_{\mathcal{B}_1} = \mathcal{O}(1)$ to hold, two conditions must be met. First, $r_n(\mathbf{x}, \mathbf{y})$ must lie in Barron-type spaces, which requires the function to have a smooth structure. This was discussed before Theorem 2 and shown to be reasonable for $r_n(\mathbf{x}, \mathbf{y})$. Second, the norm should be of order one. Based on [13, 10], we know that the H^s -norm, when $s > \frac{d}{2} + 3$, can control the Barron-type norm, and the H^s -norm can be controlled by the C^s -norm [16], where

$$\|f\|_{C^s([0,1]^d)} := \sum_{\|\boldsymbol{\alpha}\|_1 \leq s} \|\partial^{\boldsymbol{\alpha}} f\|_{C^0([0,1]^d)}.$$

When the C^s -norm has the same scale as the C^0 -norm, we can infer that when the C^0 -norm is of order one, the Barron-type norm can be controlled by an order one term. This assumption may not hold for a general target function; however, it is reasonable in our case. For the region where \mathbf{x} is close to \mathbf{y} , $\nabla \cdot (\mathbf{A}(\mathbf{x}) \nabla \phi_1(\mathbf{z}; \boldsymbol{\theta}_1))$ will reduce the high-frequency components of \mathcal{N}_ε , ensuring that in this region, the C^0 -norm is comparable to the C^s -norm. This is the motivation for establishing the large-scale neural network first. For the region where \mathbf{x} is away from \mathbf{y} , since \mathcal{N}_ε is smooth and $\nabla \cdot (\mathbf{A}(\mathbf{x}) \nabla \phi_1(\mathbf{z}; \boldsymbol{\theta}_1))$ does not explode when the activation function is local, such as $\exp(-x^2)$ or $\tanh(x)$, the C^0 -norm has also the same scale as the C^s -norm. As a result, for r_n , the C^0 -norm can have the same scale as the Barron-type norm. A rigorous proof of this assumption would require a constructive approach, rather than the existence proof presented in this paper, especially regarding how to establish $\phi_1(\mathbf{z}; \boldsymbol{\theta}_1)$ to achieve the goal stated above, and not merely meet the error bound in Theorem 1. We will explore this in future work.

Theorem 2 also shows that although various large-scale NNs can effectively reduce the approximation error of Green's functions, merely reducing the error scale does not guarantee that the small-scale NN will successfully learn the residual, particularly if the residual is not smooth and displays noise-like characteristics. Theorem 2 asserts that successful learning of the residual is more likely if it resides within the Barron-type space, suggesting a higher degree of smoothness, as outlined in [5, 34]. In practical implementations, to identify suitable large-scale NNs, we can initially train a large-scale NN to approximate the Green's function, then add a small-scale NN and finally conduct simultaneous training of both scales. This dual-scale training approach not only further refines the large-scale NN to pinpoint the correct large-scale components but also improves the small-scale NN's capacity to capture finer details, thereby ensuring thorough learning across various scales.

3.3. Training strategies. [Theorem 1](#) and [Theorem 2](#) suggest to first train the large-scale network ϕ_1 to approximately solve (2.7), i.e.,

$$(3.48) \quad \nabla \cdot (\mathbf{A}(\mathbf{x}) \nabla \phi_1) \approx \mathcal{N}_\varepsilon(\mathbf{x}, \mathbf{y}) = \left(\frac{1}{\varepsilon \sqrt{\pi}} \right)^d \exp \left(-\frac{\|\mathbf{x} - \mathbf{y}\|_2^2}{\varepsilon^2} \right).$$

Given the form of ϕ_1 defined in (3.3) and (3.4), we further have

$$(3.49) \quad \nabla \cdot (\mathbf{A}(\mathbf{x}) \nabla \phi_1) = \frac{\varepsilon^{\alpha-2}}{n} \sum_{i=1}^n \mathbf{w}_{i,\mathbf{x}}^\top \mathbf{A}(\mathbf{x}) \mathbf{w}_{i,\mathbf{x}} a_i \sigma''(\mathbf{w}_i \cdot (\varepsilon^{-1} \mathbf{x}, \varepsilon^{-1} \mathbf{y}) + \varepsilon^{-1} b_i)$$

$$(3.50) \quad + \frac{\varepsilon^{\alpha-2}}{n} \sum_{i=1}^n \varepsilon (\nabla \cdot \mathbf{A}(\mathbf{x}))^\top \mathbf{w}_{i,\mathbf{x}} \sigma'(\mathbf{w}_i \cdot (\varepsilon^{-1} \mathbf{x}, \varepsilon^{-1} \mathbf{y}) + \varepsilon^{-1} b_i).$$

In the previous section, we propose one way to choose an α in (3.44) under the condition that $\beta = 1$ for the large-scale NN. However, this choice does not yield an explicitly computable formula for α . A practical heuristic for selecting α is to ensure that the magnitude of the NN parameters has roughly the same order and is bounded, which makes the NN easier to train, particularly when ε is small, as shown in [32, 54, 67]. If all the parameters are of $\mathcal{O}(1)$, apparently it follows that $\nabla \cdot (\mathbf{A}(\mathbf{x}) \nabla \phi_1)$ is of $\mathcal{O}(\varepsilon^{\alpha-2})$. Therefore, to match the order of the right-hand side, $\mathcal{N}_\varepsilon(\mathbf{x}, \mathbf{y})$, which is $\mathcal{O}(\varepsilon^{-d})$, we should set $\alpha = 2 - d$.

The structure of the MSNN we use in practice is shown in [Figure 3.1](#), following a similar approach by Teng et al. [53]. We include an additional input feature that is the distance of coordinates \mathbf{x} and \mathbf{y} , i.e., $\mathbf{x} - \mathbf{y}$, as the value of the Green's function generally depends on the distance between \mathbf{x} and \mathbf{y} [53]. The training process begins with the training of the large-scale network, followed by a simultaneous training of both networks of the large and small scales.

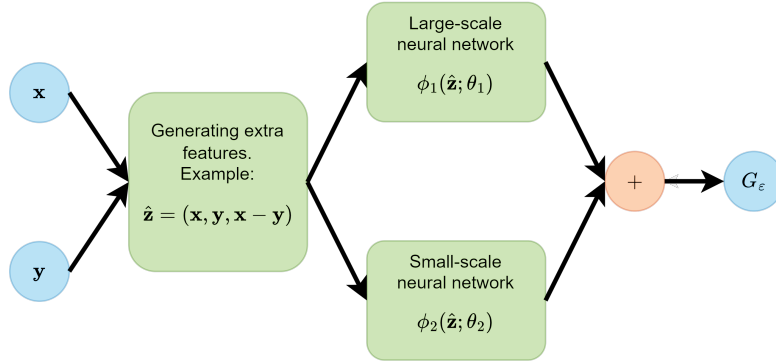


Figure 3.1: The design of the multiscale NN, incorporating $\mathbf{x} - \mathbf{y}$ as an additional feature.

As training a NN across the entire domain Ω can be challenging, we employ the domain decomposition (DD) strategy proposed by Teng et al. [53]. We divide Ω into p disjoint subdomains such that $\Omega = \bigcup \Omega_i$ for $i = 1, 2, \dots, p$, and train one NN $\phi^i((\mathbf{x}, \mathbf{y}), \boldsymbol{\theta}^i)$ for each subdomain $\Omega \times \Omega_i$. Instead of using a naive partitioning as in [53], we exploit graph partitioners as often used in general sparse matrix packages [57, 58] in order to handle general domains, by which we divide 1D domains into line segments and 2D domains into triangular elements. We denoted by \mathcal{T}_C the mesh of Ω , which does not need to be fine, as we do not need the subdomains to be perfectly balanced. The mesh \mathcal{T}_C can be associated with a graph $\mathcal{G}_C(\mathcal{V}, \mathcal{E})$, where the vertex set \mathcal{V} represents the elements in \mathcal{T}_C , and two vertices are connected by an edge in \mathcal{E} if the corresponding elements are neighbors. Then, a p -way partition with edge separators is applied to \mathcal{G}_C , dividing it into p subgraphs. Finally, a subdomain is formed by the union of the elements corresponding to the subgraph. An illustration of the DD for a rectangular domain is provided in the left panel in [Figure 3.2](#).

The training data are generated as follows. For subdomain i , we sample a few points $S^i \in \Omega_i$, and for each $\mathbf{y} \in S^i$, we sample \mathbf{x} points to form the following sets of (\mathbf{x}, \mathbf{y}) pair: 1) $S_{\mathbf{y}, bdr}^i$ with \mathbf{x} on the domain boundary $\partial\Omega$; 2) $S_{\mathbf{y}, far}^i$ with \mathbf{x} uniformly distributed within the domain Ω ; and 3)

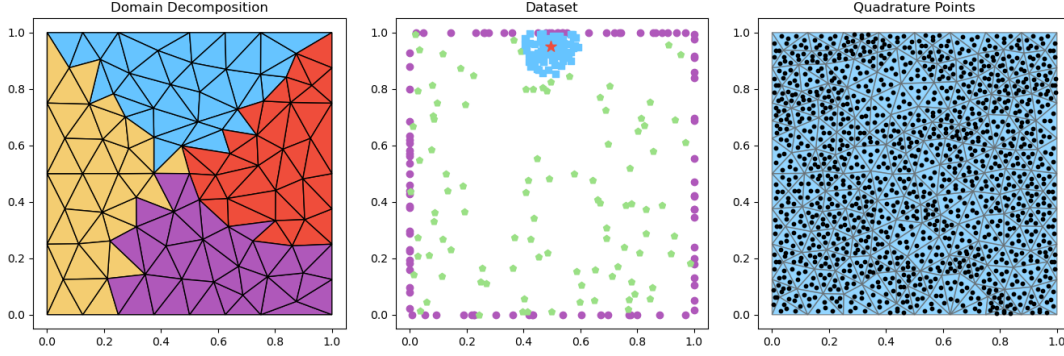


Figure 3.2: DD, dataset, and quadrature points in a rectangular domain. Left: DD using a coarse mesh \mathcal{T}_C and 4-way graph partitioning. Middle: dataset with \mathbf{y} from one subdomain (the red star), \mathbf{x} close to \mathbf{y} (the blue squares), \mathbf{x} uniformly sampled in Ω (the green pentagon), and \mathbf{x} on boundary (the purple dots). Right: Quadrature points (the black dots) used in a fine mesh \mathcal{T}_F .

$S_{\mathbf{y},near}^i$ with \mathbf{x} uniformly distributed within a predefined radius from \mathbf{y} in the domain Ω . The dataset associated with i -th subdomain is constructed as

$$(3.51) \quad S_{bdry}^i := \cup_{\mathbf{y} \in S^i} S_{\mathbf{y},bdry}^i$$

$$(3.52) \quad S_{int}^i := (\cup_{\mathbf{y} \in S^i} S_{\mathbf{y},near}^i) \cup (\cup_{\mathbf{y} \in S^i} S_{\mathbf{y},far}^i),$$

where S_{bdry}^i are data points on the boundary and S_{int}^i are data points within the domain. The data points sampled associated with one \mathbf{y} are illustrated in the middle panel in Figure 3.2.

Defined on these data points, the loss function L^i on the i -th subdomain is defined as

$$(3.53) \quad L^i = w_{bdry} L_{bdry}^i + w_{res} L_{res}^i + w_{sym} L_{sym}^i,$$

which was first proposed in [53], where

$$(3.54) \quad L_{bdry}^i(\boldsymbol{\theta}^i) = \frac{1}{|S_{bdry}^i|} \sum_{(\mathbf{x}, \mathbf{y}) \in S_{bdry}^i} \phi^i((\mathbf{x}, \mathbf{y}), \boldsymbol{\theta}^i)^2$$

$$(3.55) \quad L_{res}^i(\boldsymbol{\theta}^i) = \frac{1}{|S_{int}^i|} \sum_{(\mathbf{x}, \mathbf{y}) \in S_{int}^i} [\mathcal{L}\phi^i((\mathbf{x}, \mathbf{y}), \boldsymbol{\theta}^i) - \mathcal{N}_\varepsilon(\mathbf{x}, \mathbf{y})]^2$$

$$(3.56) \quad L_{sym}^i(\boldsymbol{\theta}^i) = \frac{1}{|S_{int}^i|} \sum_{(\mathbf{x}, \mathbf{y}) \in S_{int}^i} [\phi^i((\mathbf{x}, \mathbf{y}), \boldsymbol{\theta}^i) - \phi^i((\mathbf{y}, \mathbf{x}), \boldsymbol{\theta}^i)]^2.$$

Here, L_{bdry}^i represents the error on the boundary, L_{res}^i measures the point-wise residual of the PDE, and L_{sym}^i is designed to ensure the symmetry $\phi^i(x, y) = \phi^i(y, x)$. The weight terms w_{bdry} , w_{res} , and w_{sym} are used to balance these loss terms. The NNs on those subdomains are trained independently in parallel.

After the model is trained, numerical integration is computed for the final solution. The quadrature points are selected from a much finer mesh of the domain Ω , which is denoted by \mathcal{T}_F . The numerical integration uses the Gauss-Legendre rule for line segments and Dunavant's integration rules for triangular elements [12].

The overall procedure for solving PDE problems using the multiscale NN learning approach is illustrated in Figure 3.3. Before concluding this section, it is worth noting that the analysis can be easily generalized to more complex linear differential operators. In section 4, we present numerical examples with more intricate operators to demonstrate the effectiveness of our method.

4. Numerical Experiments. This section outlines the experiments conducted using our MSNN approach to approximate Green's functions. We specifically compare the performance of our multiscale model (in the form of $\phi_1 + \phi_2$) to the single scale models (in the form of ϕ_1 or ϕ_2 alone) for various problems, including convergence in the training process and prediction accuracy. The following notations are adopted in this section:

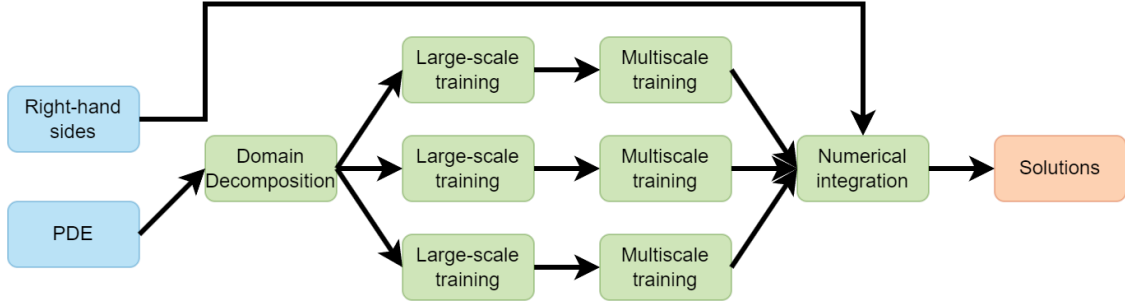


Figure 3.3: The overall procedure of solving PDEs by the multiscale NN learning approach for Green’s function. A large-scale network in each subdomain is first trained, and both the large- and small-scale NNs in the subdomain are trained together. The PDE solution is computed by numerical integration with the learned Green’s function and the right-hand-side function of the PDE.

- ϕ^l : the standalone large-scale network model.
- ϕ^s : the standalone small-scale network model.
- ϕ_1^m : the large-scale network within the multiscale framework.
- ϕ_2^m : the small-scale network within the multiscale framework.
- ϕ^m : the multiscale network (combined output of ϕ_1^m and ϕ_2^m).

Our experiment code was developed using `Python` with `PyTorch` [42] for the NN implementations and `NumPy` [21] for data generation. All the NNs used in our experiments are fully connected with linear layers and the \tanh activation function. The experiments were conducted on a machine equipped with dual 24-core 2.1 GHz Intel Xeon Gold 5318Y CPUs, an NVIDIA H100 GPU, and 1 TB of RAM. The versions of the main software/libraries used were `Python` 3.8.19, `PyTorch` 2.2.2, `NumPy` 1.24.3, and `CUDA` 12.5. Triangular elements were generated using the `MeshPy` package [29], and we implemented a simple spectral graph partitioning algorithm for graph partitioning. When sampling data, the radius for sampling “near points” is set at 2ε . In all the experiments, we fix the loss weights w_{res} to 1.0 and set $w_{bdry} = w_{sym} = \varepsilon^{-d}$.

4.1. Model Problems. We consider the following model problem:

$$(4.1) \quad \begin{cases} -\Delta u(\mathbf{x}) - c(\mathbf{x})u(\mathbf{x}) = f(\mathbf{x}), & \mathbf{x} \in \Omega \\ u(\mathbf{x}) = 0, & \mathbf{x} \in \partial\Omega \end{cases}$$

We explore various domains Ω in \mathbb{R} and \mathbb{R}^2 , with different functions $c(\mathbf{x})$ from \mathbb{R}^d to \mathbb{R} . We benchmark our network’s performance by comparing the numerical solutions obtained from our trained networks against those derived using the Finite Element Method (FEM) with linear elements. These comparisons are facilitated using the `FEniCS` package for FEM [3, 33]. We refine the mesh \mathcal{T}_F using `FEniCS` and obtain numerical solutions of high accuracy for comparison.

4.2. Selection of ε . Before testing our framework, we first study the influence of ε on the approximation accuracy of the Green’s function since we are using $\mathcal{N}_\varepsilon(\mathbf{x}, \mathbf{y})$ as the approximation of $\delta(\mathbf{x}, \mathbf{y})$.

In [Figure 4.1](#) and [Figure 4.2](#), we compare the approximations using various ε with the exact Green’s function for the 1-D problem with $c = 0$ on $\Omega = [0, 1]$. The exact Green’s function is given by

$$(4.2) \quad G(x, y) = \begin{cases} x(1 - y), & x < y \\ y(1 - x), & x \geq y. \end{cases}$$

We first fix $y = 0.95$ and compare the exact $G(x, 0.95)$ with the approximations obtained from FEM and various ε . As shown in [Figure 4.1](#), the approximation with $\varepsilon = 10^{-2}$ is very close to the true solution, whereas larger ε values cannot yield accurate enough approximations. In [Figure 4.2](#), we plot the entire Green’s function. Again, a good approximation can be obtained with $\varepsilon = 10^{-2}$.

Next, we show the Green’s function for 2-D problems on a unit circle with fixed $\mathbf{y} = (0.5, 0.5)$. As we can see from [Figure 4.3](#), it is necessary to use a small ε (e.g., lower than 0.02) to obtain a good

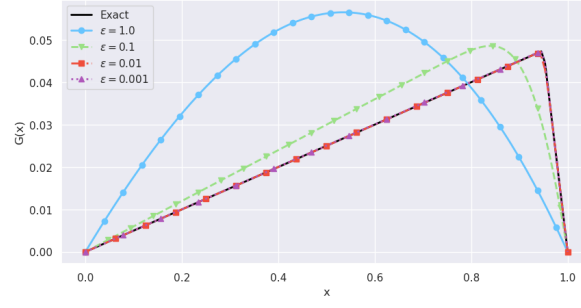


Figure 4.1: FEM Green's function approximations at $y = 0.95$ using $\varepsilon = 1.0, 0.1, 0.01, 0.001$ for the 1-D problem (4.1) with $c = 0$ on $\Omega = [0, 1]$.

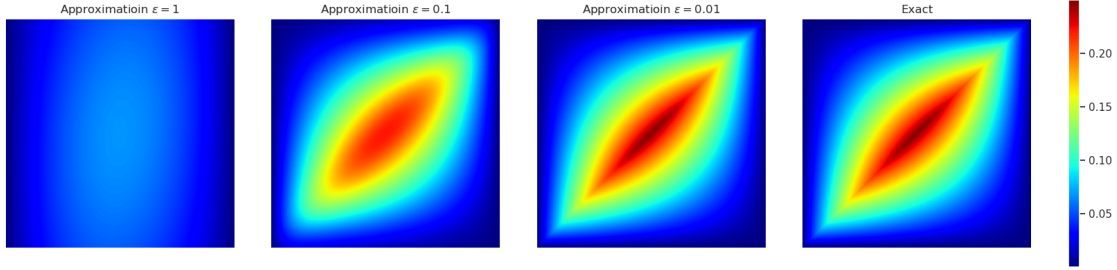


Figure 4.2: FEM Green's function approximations using $\varepsilon = 1.0, 0.1, 0.01$ for the 1-D problem (4.1) with $c = 0$ on $\Omega = [0, 1]$. The x-axis is the x values, and y-axis is the y values.

approximation. In our tests, we use $\varepsilon = 0.01$ for 1D problems and $\varepsilon = 0.02$ for 2D problems, unless otherwise noted.

4.3. Magnitude of Network Parameters. In our next experiment, we allow all networks to undergo enough Adam steps to reach a certain accuracy. We plot the histogram of network parameters for each network to justify that we are able to find a multiscale network such that the parameters are bounded with respect to ε . We run a simple test with $c(x) = 1 + x^2$ on $\Omega = [0, 1]$ with zero boundary condition and only learn the Green's function at a fixed $y = 0.95$. We choose this simple problem because it is difficult to train the standalone small-scale network ϕ^s to converge to a reasonable accuracy for more challenging problems. In this test, the NNs are configured with just one hidden layer to align with the theoretical expectations. For multiscale network ϕ^m , both the large-scale network ϕ_1^m and the small-scale network ϕ_2^m utilize a hidden layer of 100 neurons. The standalone networks ϕ^l and ϕ^s are equipped with a hidden layer comprising 200 neurons, ensuring that the total number of parameters in ϕ^m , ϕ^l and ϕ^s remains close for a fair comparison. We run Adam and check the error every 20,000 iterations until the l_∞ error on the testing set is smaller than 0.01, which means that the network has a reasonable accuracy. We test multiple ε values from 0.01 to 1.0. The results are shown in Figure 4.4.

As shown in the figure, the multiscale network ϕ^m exhibits consistent parameter distribution across all the ε values, with minimal variation in the extreme values of the model parameters. The large-scale network alone demonstrates similar behavior. For large ε , the parameter distributions of the large-scale model ϕ^l are comparable to those of the multiscale network. However, when ε becomes small (e.g., $\varepsilon = 0.01$), the model parameters contain a few larger values compared to the multiscale network. In contrast, a well-trained small-scale network ϕ^s requires many large parameter values to represent a good approximation when ε is small, posing significant challenges for training. In fact, over 10^6 iterations of Adam were required for ϕ^s to converge with $\varepsilon = 0.01$, while 20,000 iterations is more than enough for ϕ^l and ϕ^m . Finally, we note in passing that ϕ^l and ϕ^s are equivalent when $\varepsilon = 1.0$.

4.4. Test with Fixed y . In the previous sections, we justified the selection of ε values in our experiments and studied the distribution of model parameters after the model converges. In the fol-

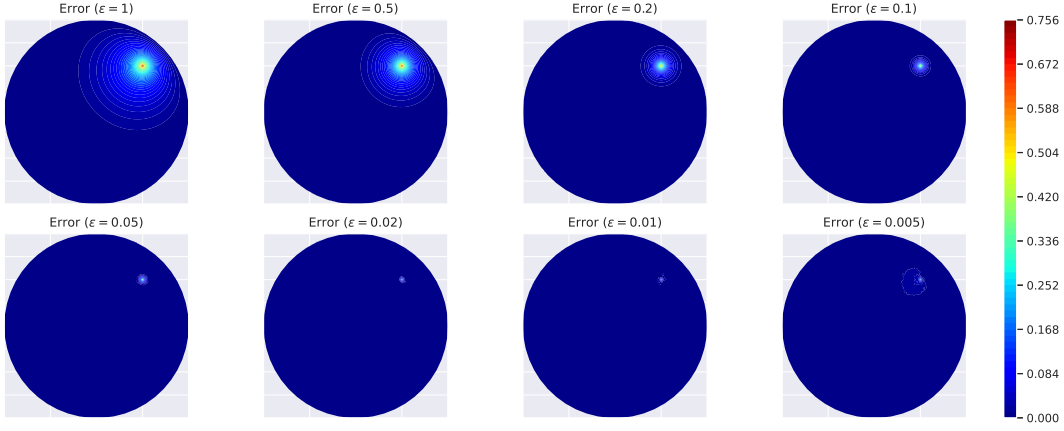


Figure 4.3: Difference between the FEM solution of Green's function approximation and the exact Green's function for the 2-D problem (4.1) in a unit circle with $c = 0$ at $\mathbf{y} = (0.5, 0.5)$.

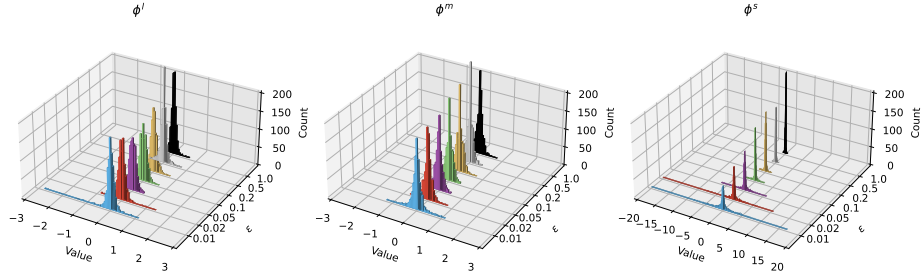


Figure 4.4: Histogram of model parameters for trained networks on a line segment with $c(x) = 1 + x^2$, $y = 0.95$, and varying ε . The parameter distributions for ϕ^l and ϕ^m remain relatively stable as ε changes, whereas the parameter distribution for the small-scale network ϕ^s varies significantly. For small ε , ϕ^s requires larger parameters, making it more difficult to train.

lowing experiments, we focus on demonstrating that our multiscale network is easier to train compared to single scale models.

Our next group of experiments are still designed to test convergence with a fixed \mathbf{y} . Specifically, we train the network to approximate $G(\mathbf{x}, \mathbf{y})$ for $\mathbf{x} \in \Omega$ and a single predetermined \mathbf{y} . We start with the 1D problem (4.1) with $\Omega = [0, 1]$ and $c = 0, 1$, and $1 + x^2$, selecting y values at 0.5, 0.7, and 0.95. These points were chosen to represent the center, typically internal points, and near-boundary points of the domain, respectively. For the simple case where $c = 0$, both the large-scale network ϕ_1^m and the small-scale network ϕ_2^m in the multiscale network ϕ^m utilize a hidden layer of 20 neurons. The single scale networks ϕ^l and ϕ^s are equipped with a hidden layer comprising 40 neurons. For the cases where $c = 1$ and $c = 1 + x^2$, we increase the number of neurons on the hidden layer to 100 for ϕ^l and ϕ^s , and set the number of neurons on the hidden layer to 50 for ϕ_1^m and ϕ_2^m . During training, only one value of y is sampled per test, along with two boundary points at 0 and 1. Additionally, we uniformly sample 500 points across $[0, 1]$ and sample 500 points near the selected \mathbf{y} , as previously discussed. The training regimen for ϕ^m involves 1,000 steps for the large-scale network ϕ_1^m , followed by 4,000 steps for the entire network. In contrast, the baseline ϕ^l and ϕ^s undergoes a longer training of 5,000 steps, resulting in a higher total computational cost, as training ϕ_1^m is much cheaper per step. In this test, we set $\varepsilon = 10^{-2}$. For $c = 1$ and $c = 1 + x^2$, we use a fine mesh to compute a high-accuracy FEM solution as the true solution. In order to make a fair comparison, we apply the grid search on the initial learning rate and the decay rate for each model and report the result with the minimum error

in the tests. We search for the initial learning rate from 10^{-4} to 10^{-1} , and search for the decay rate from 0.9 to 1.0 where the decay is applied every 500 iterations. These comparisons are depicted in Figure 4.5.

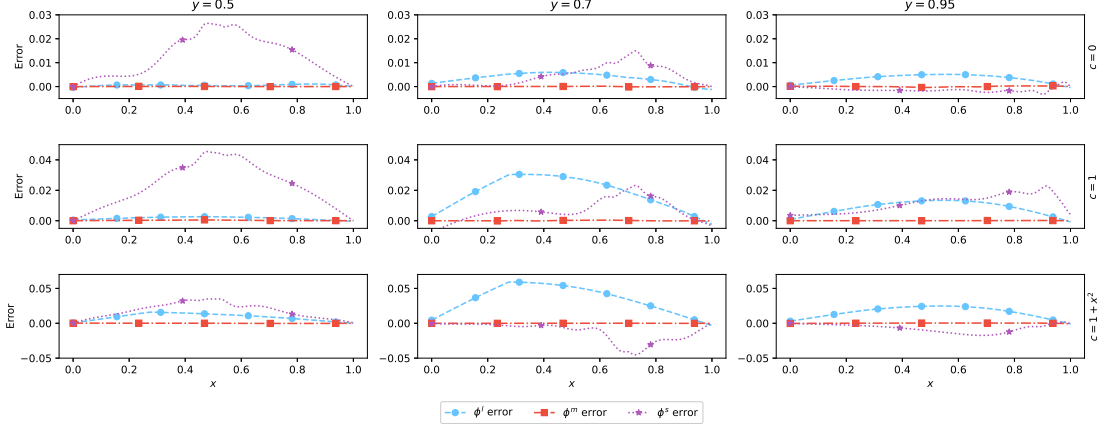


Figure 4.5: Approximation error comparison of three trained networks ϕ^l , ϕ^m and ϕ^s on $\Omega = [0, 1]$ at fixed y , with three cases of $c(x) = 0, 1$, and $1 + x^2$. The reference solution is taken as a high-accuracy FEM solution computed on a fine mesh for $c(x) = 1.0$ and $c(x) = 1 + x^2$. ϕ^l , ϕ^m and ϕ^s have roughly the same number of parameters and are trained with the same number of epochs.

The figures show that the single-scale networks ϕ^l and ϕ^s not only incur higher training costs but also exhibit slower convergence compared to the multiscale network ϕ^m . Notably, even after 5,000 iterations, the predictions of ϕ^s remain far from the exact Green's function. The standalone large-scale network ϕ^l performs well when $c = 0$ and $y = 0.5$, but its predictions worsen in other cases. In contrast, the multiscale network consistently delivers better predictions across all experiments at a lower cost. This evidence highlights the superior convergence capabilities of multiscale networks.

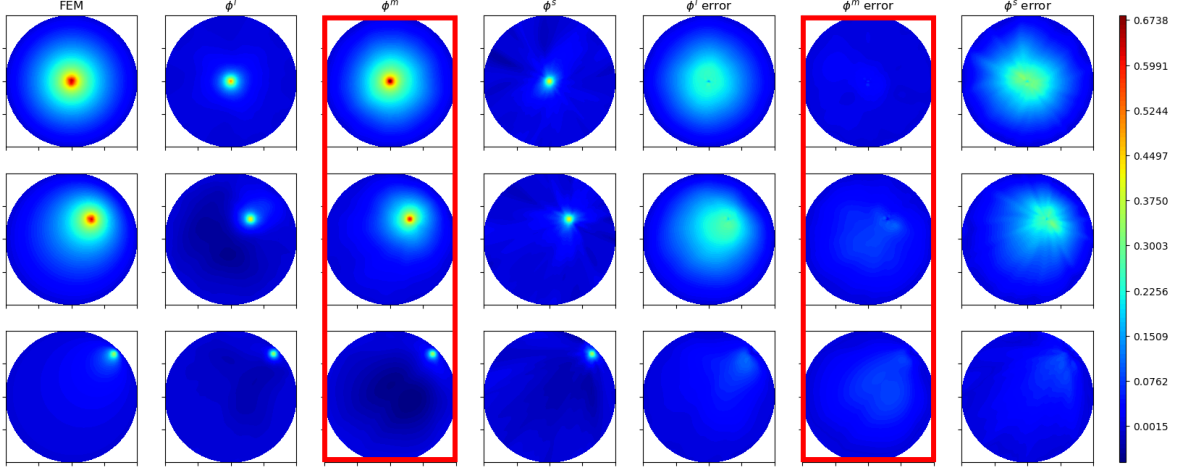


Figure 4.6: Approximation accuracy comparison for three trained networks ϕ^l , ϕ^m and ϕ^s on a unit circle at three fixed $\mathbf{y} = (0,0)$, $(0.3,0.3)$, and $(0.65,0.65)$ with $c(\mathbf{x}) = 1 + x_1^2 + x_2^2$. The reference solution is taken as a high-accuracy FEM solution computed on a fine mesh. The results of ϕ^m are highlighted using red boxes. ϕ^l , ϕ^m and ϕ^s have roughly the same number of parameters and are trained with the same number of epochs.

Next, we conduct our tests in a 2-D unit circle domain with fixed points $\mathbf{y} = (0,0)$, $(0.3,0.3)$, and $(0.65,0.65)$. For this set of tests, we use $c(\mathbf{x}) = 1 + x_1^2 + x_2^2$. Since this problem is more challenging, we

employ networks with two hidden layers. The number of neurons in each hidden layer is set to 50 for ϕ^l and ϕ^s , and 30 for ϕ_1^m and 40 for ϕ_2^m . We sample 500 points on the boundary, 5,000 points near \mathbf{y} , and 5,000 points uniformly across the entire domain. For the MSNN, we first train ϕ_1^m for 2,000 steps, followed by training the full ϕ^m for 8,000 steps. For the single-scale networks, ϕ^l and ϕ^s are trained for 10,000 steps. The learning rate is set to 10^{-3} in this test. As shown in Figure 4.6, our multiscale network consistently provides better predictions.

4.5. Test on Solution of PDEs. Finally, we evaluate our complete MSNN framework by solving PDEs. We revisit the 1D model problem on the interval $[0, 1]$ with $c = 1 + x^2$. For this test, we partition the interval into 32 subdomains and set $\varepsilon = 0.01$. Each subdomain samples 30 different y values; for each y , we associate 2 boundary points, 500 uniformly distributed points within the domain, and 500 points close to y . We use networks with two hidden layers, with 50 neurons per layer for ϕ^l and ϕ^s , 30 neurons for ϕ_1^m , and 40 for ϕ_2^m . The large-scale model ϕ_1^m is first trained for 4,000 iterations, followed by an additional 16,000 iterations to train the full multiscale network. In contrast, the baseline networks, ϕ^s and ϕ^l , are trained for 20,000 iterations. As shown in Figure 4.7, the results clearly demonstrate that the multiscale network achieves significantly better performance.

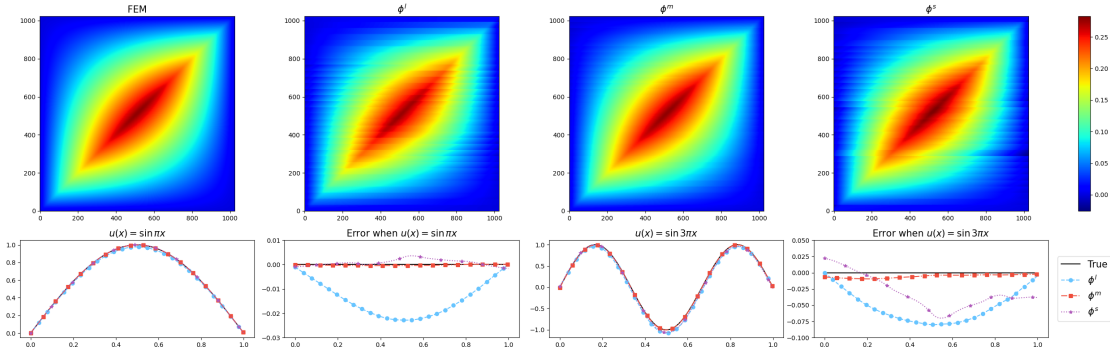


Figure 4.7: Predicted Green's function and numerical solutions of PDEs. Upper: comparison between predicted Green's function and a high accuracy FEM solution. Lower: comparison between solutions and error when solving PDEs with solutions $u(x) = \sin(\pi x)$ and $u(x) = \sin(3\pi x)$. Here we choose $c(x) = 1 + x^2$.

We further validate the accuracy of our approximation by solving PDEs with specified right-hand sides. Specifically, we test our approach using PDEs with solutions $u(x) = \sin(\pi x)$ and $u(x) = \sin(3\pi x)$. We then compare the exact solutions with the numerical solutions derived from the approximated Green's function. As shown in Figure 4.7, our network's output provides significantly better approximations to the true solution in both cases.

Next, we extend our investigations to high-dimensional problems. In the upcoming experiment, we address 2D model problems on the domains $[-1, 1]^2$ and the unit circle, with $c(\mathbf{x}) = 1 + x_1^2 + x_2^2$. For this test, the domain is divided into 32 subdomains, and ε is set to 0.02. We use networks with three hidden layers, with 50 neurons per layer for ϕ^l and ϕ^s , 30 neurons for ϕ_1^m , and 40 for ϕ_2^m . When generating the datasets, 50 values of \mathbf{y} are selected, each associated with 20 boundary points, 200 uniformly distributed points within the domain, and 200 additional points near \mathbf{y} .

Each large-scale model within the multiscale network ϕ^m is trained for 10,000 iterations, followed by 40,000 iterations for the full multiscale network. In comparison, the baseline single-scale networks ϕ^s and ϕ^l are trained for 50,000 iterations. We assess the effectiveness of our approximation using PDEs with solutions $u(\mathbf{x}) = \sin(\pi x_1) \sin(\pi x_2)$ and $u(\mathbf{x}) = \sin(3\pi x_1) \sin(3\pi x_2)$ for the rectangular domain, and $u(\mathbf{x}) = 1 - x_1^2 - x_2^2$ and $u(\mathbf{x}) = (1 - x_1^2 - x_2^2) \sin(3\pi x_1) \sin(3\pi x_2)$ for the unit circle domain. The results, shown in Figure 4.8, demonstrate that our network achieves a much closer approximation to the true solution with significantly lower training costs, highlighting the efficiency of our framework.

5. Conclusion. In this paper, we propose a multiscale NN approach to learn Green's functions to solve PDE problems, consisting of both low-regularity and high-regularity components. We found that, compared to regular NNs, our approach requires fewer parameters and maintains the boundedness of the model parameters. Therefore, it can reduce training complexity and significantly speed up the

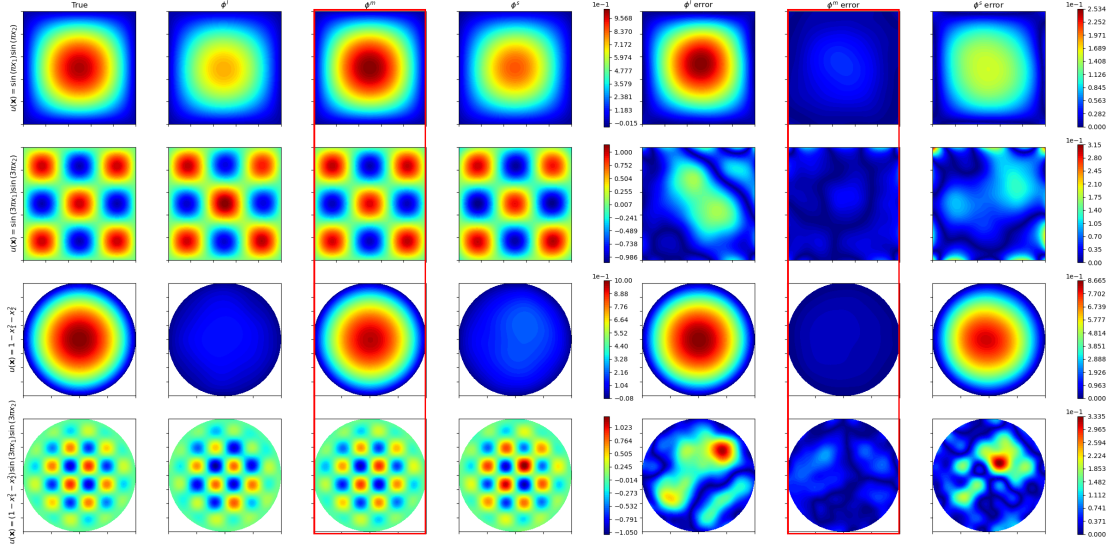


Figure 4.8: 2D model problem with $c(\mathbf{x}) = 1 + x_1^2 + x_2^2$. The exact solutions in the first column are $u(\mathbf{x}) = \sin(\pi x_1) \sin(\pi x_2)$ and $u(\mathbf{x}) = \sin(3\pi x_1) \sin(3\pi x_2)$ for the rectangular domain, and $u(\mathbf{x}) = 1 - x_1^2 - x_2^2$ and $u(\mathbf{x}) = (1 - x_1^2 - x_2^2) \sin(3\pi x_1) \sin(3\pi x_2)$ for the unit circle domain. Solutions obtained from different neural network frameworks are presented in the subsequent columns. The solutions from the multiscale network ϕ^m are highlighted with red boxes.

training process, as demonstrated by both theoretical analysis and experimental performance. With the proposed approach, Green's functions can be approximated more effectively than a single-scale NN because the large-scale NN can capture the large-scale (low-regularity) part and the small-scale neural networks is to approximate the residual high-regularity components.

While the theoretical results provide an existence proof for multiscale neural networks, a constructive proof would be valuable to verify the underlying assumptions and assist in designing neural networks for experimental purposes. We view this as a promising direction for future research. Furthermore, we intend to utilize the neural network approximation of the Green's function to develop more parallel and robust preconditioners than those based on sequential ILU factorizations [59] for solving highly indefinite problems, such as high-frequency wave equations in our future work.

REFERENCES

- [1] R. ADAMS AND J. FOURNIER, *Sobolev spaces*, Elsevier, 2003.
- [2] M. AINSWORTH AND Y. SHIN, *Active neuron least squares: A training method for multivariate rectified neural networks*, SIAM Journal on Scientific Computing, 44 (2022), pp. A2253–A2275.
- [3] M. ALNÆS, J. BLECHTA, J. HAKE, A. JOHANSSON, B. KEHLET, A. LOGG, C. RICHARDSON, J. RING, M. E. Rognes, AND G. N. WELLS, *The fenics project version 1.5*, Archive of numerical software, 3 (2015).
- [4] M. ANTHONY, P. BARTLETT, ET AL., *Neural network learning: Theoretical foundations*, vol. 9, cambridge university press Cambridge, 1999.
- [5] A. BARRON, *Universal approximation bounds for superpositions of a sigmoidal function*, IEEE Transactions on Information theory, 39 (1993), pp. 930–945.
- [6] M. BEBENDORF AND W. HACKBUSCH, *Existence of \mathcal{H} -matrix approximants to the inverse fe-matrix of elliptic operators with L^∞ -coefficients*, Numerische Mathematik, 95 (2003), pp. 1–28.
- [7] N. BOULLÉ AND A. TOWNSEND, *Learning elliptic partial differential equations with randomized linear algebra*, Foundations of Computational Mathematics, 23 (2023), pp. 709–739.
- [8] J. CHEN, X. CHI, Z. YANG, ET AL., *Bridging traditional and machine learning-based algorithms for solving pdes: the random feature method*, J Mach Learn, 1 (2022), pp. 268–98.
- [9] Q. CHEN AND W. HAO, *Randomized newton's method for solving differential equations based on the neural network discretization*, Journal of Scientific Computing, 92 (2022), p. 49.
- [10] Z. CHEN, J. LU, AND Y. LU, *On the representation of solutions to elliptic pdes in barron spaces*, Advances in neural information processing systems, 34 (2021), pp. 6454–6465.
- [11] S. DONG AND Y. WANG, *A method for computing inverse parametric pde problems with random-weight neural networks*, Journal of Computational Physics, 489 (2023), p. 112263.
- [12] D. DUNAVANT, *High degree efficient symmetrical gaussian quadrature rules for the triangle*, International journal

- for numerical methods in engineering, 21 (1985), pp. 1129–1148.
- [13] W. E AND S. WOJNOWYTSCH, *Representation formulas and pointwise properties for barron functions*, Calculus of Variations and Partial Differential Equations, 61 (2022), p. 46.
 - [14] W. E AND S. WOJNOWYTSCH, *Some observations on high-dimensional partial differential equations with barron data*, in Mathematical and Scientific Machine Learning, PMLR, 2022, pp. 253–269.
 - [15] W. E AND B. YU, *The Deep Ritz Method: A deep learning-based numerical algorithm for solving variational problems*, Communications in Mathematics and Statistics, 6 (2018).
 - [16] L. EVANS, *Partial differential equations*, vol. 19, American Mathematical Society, 2022.
 - [17] Y. FAN, L. LIN, L. YING, AND L. ZEPEDA-NÚÑEZ, *A multiscale neural network based on hierarchical matrices*, Multiscale Modeling & Simulation, 17 (2019), pp. 1189–1213.
 - [18] C. GIN, D. SHEA, S. BRUNTON, AND J. N. KUTZ, *Deepgreen: deep learning of green's functions for nonlinear boundary value problems*, Scientific reports, 11 (2021), p. 21614.
 - [19] I. GÜHRING AND M. RASLAN, *Approximation rates for neural networks with encodable weights in smoothness spaces*, Neural Networks, 134 (2021), pp. 107–130.
 - [20] W. HAO, Q. HONG, AND X. JIN, *Gauss newton method for solving variational problems of pdes with neural network discretizations*, Journal of Scientific Computing, 100 (2024), p. 17.
 - [21] C. R. HARRIS, K. J. MILLMAN, S. J. VAN DER WALT, R. GOMMERS, P. VIRTANEN, D. COUNAPEAU, E. WIESER, J. TAYLOR, S. BERG, N. J. SMITH, R. KERN, M. PICUS, S. HOYER, M. H. VAN KERKWIJK, M. BRETT, A. HALDANE, J. F. DEL RÍO, M. WIEBE, P. PETERSON, P. GÉRARD-MARCHANT, K. SHEPPARD, T. REDDY, W. WECKESSER, H. ABBASI, C. GOHLKE, AND T. E. OLIPHANT, *Array programming with NumPy*, Nature, 585 (2020), pp. 357–362.
 - [22] H. HE, Z. TANG, S. ZHAO, Y. SAAD, AND Y. XI, *nltgr: A class of nonlinear acceleration procedures based on conjugate residuals*, SIAM Journal on Matrix Analysis and Applications, 45 (2024), pp. 712–743.
 - [23] K. HE, X. ZHANG, S. REN, AND J. SUN, *Delving deep into rectifiers: Surpassing human-level performance on imagenet classification*, in Proceedings of the IEEE international conference on computer vision, 2015, pp. 1026–1034.
 - [24] F. HILDEBRAND, *Introduction to numerical analysis*, Courier Corporation, 1987.
 - [25] A. HOWARD, M. PEREGO, G. KARNIAKAKIS, AND P. STINIS, *Multifidelity deep operator networks for data-driven and physics-informed problems*, Journal of Computational Physics, 493 (2023), p. 112462.
 - [26] J. JI, L. JU, AND X. ZHANG, *Deep surrogate model for learning green's function associated with linear reaction-diffusion operator*, arXiv preprint arXiv:2310.03642, (2023).
 - [27] D. KINGMA AND J. BA, *Adam: A method for stochastic optimization*, arXiv preprint arXiv:1412.6980, (2014).
 - [28] D. KINGMA AND J. BA, *Adam: A method for stochastic optimization*, in International Conference on Learning Representations (ICLR), San Diego, CA, USA, 2015.
 - [29] A. KLOECKNER, *Meshpy: Simplicial mesh generation from python*, 2018.
 - [30] Z. LI, N. KOVACHKI, K. AZIZZADENESHELI, B. LIU, K. BHATTACHARYA, A. STUART, AND A. ANANDKUMAR, *Fourier neural operator for parametric partial differential equations*, arXiv preprint arXiv:2010.08895, (2020).
 - [31] G. LIN, F. CHEN, P. HU, X. CHEN, J. CHEN, J. WANG, AND Z. SHI, *A neural network framework for learning green's function*, (2021).
 - [32] Z. LIU, W. CAI, AND Z. XU, *Multi-scale deep neural network (mscalednn) for solving poisson-boltzmann equation in complex domains*, arXiv preprint arXiv:2007.11207, (2020).
 - [33] A. LOGG, K.-A. MARDAL, AND G. WELLS, *Automated solution of differential equations by the finite element method: The FEniCS book*, vol. 84, Springer Science & Business Media, 2012.
 - [34] J. LU, Y. LU, AND M. WANG, *A priori generalization analysis of the Deep Ritz method for solving high dimensional elliptic partial differential equations*, in Conference on Learning Theory, PMLR, 2021, pp. 3196–3241.
 - [35] L. LU, P. JIN, G. PANG, Z. ZHANG, AND G. E. KARNIAKAKIS, *Learning nonlinear operators via deepnet based on the universal approximation theorem of operators*, Nature Machine Intelligence, 3 (2019), pp. 218 – 229.
 - [36] T. LUO AND H. YANG, *Two-layer neural networks for partial differential equations: Optimization and generalization theory*, arXiv preprint arXiv:2006.15733, (2020).
 - [37] C. MA, S. WOJNOWYTSCH, L. WU, ET AL., *Towards a mathematical understanding of neural network-based machine learning: what we know and what we don't*, arXiv preprint arXiv:2009.10713, (2020).
 - [38] C. MA, L. WU, ET AL., *The barron space and the flow-induced function spaces for neural network models*, Constructive Approximation, 55 (2022), pp. 369–406.
 - [39] H. MONTANELLI AND Q. DU, *New error bounds for deep relu networks using sparse grids*, SIAM Journal on Mathematics of Data Science, 1 (2019), pp. 78–92.
 - [40] S. NAH, T. HYUN KIM, AND K. MU LEE, *Deep multi-scale convolutional neural network for dynamic scene deblurring*, in Proceedings of the IEEE conference on computer vision and pattern recognition, 2017, pp. 3883–3891.
 - [41] M. NEWMAN AND G. BARKEMA, *Monte Carlo methods in statistical physics*, Clarendon Press, 1999.
 - [42] A. PASZKE, S. GROSS, F. MASSA, A. LERER, J. BRADBURY, G. CHANAN, T. KILLEEN, Z. LIN, N. GIMELSHEIN, L. ANTIGA, A. DESMAISON, A. KOPF, E. YANG, Z. DEVITO, M. RAISON, A. TEJANI, S. CHILAMKURTHY, B. STEINER, L. FANG, J. BAI, AND S. CHINTALA, *Pytorch: An imperative style, high-performance deep learning library*, in Advances in Neural Information Processing Systems, H. Wallach, H. Larochelle, A. Beygelzimer, F. d'Alché-Buc, E. Fox, and R. Garnett, eds., vol. 32, Curran Associates, Inc., 2019.
 - [43] M. RAISSI, P. PERDIKARIS, AND G. KARNIAKAKIS, *Physics-informed neural networks: A deep learning framework for solving forward and inverse problems involving nonlinear partial differential equations*, Journal of Computational Physics, 378 (2019), pp. 686–707.
 - [44] J. SCHMIDT-HIEBER, *Nonparametric regression using deep neural networks with relu activation function*, (2020).
 - [45] S. SHALEV-SHWARTZ AND S. BEN-DAVID, *Understanding machine learning: From theory to algorithms*, Cambridge university press, 2014.
 - [46] J. SIEGEL, *Optimal approximation rates for deep ReLU neural networks on Sobolev spaces*, arXiv preprint arXiv:2211.14400, (2022).

- [47] J. SIEGEL, Q. HONG, X. JIN, W. HAO, AND J. XU, *Greedy training algorithms for neural networks and applications to pdes*, Journal of Computational Physics, 484 (2023), p. 112084.
- [48] J. SIEGEL AND J. XU, *Sharp bounds on the approximation rates, metric entropy, and n -widths of shallow neural networks*, Foundations of Computational Mathematics, (2022), pp. 1–57.
- [49] J. SIEGEL AND J. XU, *Characterization of the variation spaces corresponding to shallow neural networks*, Constructive Approximation, 57 (2023), pp. 1109–1132.
- [50] J. SIRIGNANO AND K. SPILIOPOULOS, *Dgm: A deep learning algorithm for solving partial differential equations*, Journal of computational physics, 375 (2018), pp. 1339–1364.
- [51] J. SUN, S. DONG, AND F. WANG, *Local randomized neural networks with discontinuous galerkin methods for partial differential equations*, Journal of Computational and Applied Mathematics, 445 (2024), p. 115830.
- [52] T. SUZUKI, *Adaptivity of deep relu network for learning in besov and mixed smooth besov spaces: optimal rate and curse of dimensionality*, arXiv preprint arXiv:1810.08033, (2018).
- [53] Y. TENG, X. ZHANG, Z. WANG, AND L. JU, *Learning green's functions of linear reaction-diffusion equations with application to fast numerical solver*, in Mathematical and Scientific Machine Learning, PMLR, 2022, pp. 1–16.
- [54] B. WANG, W. ZHANG, AND W. CAI, *Multi-scale deep neural network (mscalednn) methods for oscillatory stokes flows in complex domains*, arXiv preprint arXiv:2009.12729, (2020).
- [55] K. WIMALAWARNE, T. SUZUKI, AND S. LANGER, *Learning Green's function efficiently using low-rank approximations*, arXiv preprint arXiv:2308.00350, (2023).
- [56] S. WOJTOWYTSCH AND W. E, *Representation formulas and pointwise properties for barron functions*, Calculus of Variations and Partial Differential Equations, 61 (2022), pp. 1–37.
- [57] T. XU, A. AUSTIN, V. KALANTZIS, AND Y. SAAD, *A parallel algorithm for computing partial spectral factorizations of matrix pencils via chebyshev approximation*, SIAM Journal on Scientific Computing, 46 (2024), pp. S324–S351.
- [58] T. XU, V. KALANTZIS, R. LI, Y. XI, G. DILLON, AND Y. SAAD, *pargemslr: A parallel multilevel schur complement low-rank preconditioning and solution package for general sparse matrices*, Parallel Comput., 113 (2022).
- [59] T. XU, R. LI, AND D. OSEI-KUFFUOR, *A two-level gpu-accelerated incomplete lu preconditioner for general sparse linear systems*, arXiv preprint arXiv:2303.08881, (2023).
- [60] Y. YANG, Q. CHEN, AND W. HAO, *Homotopy relaxation training algorithms for infinite-width two-layer relu neural networks*, arXiv preprint arXiv:2309.15244, (2023).
- [61] Y. YANG AND J. HE, *Deeper or wider: A perspective from optimal generalization error with sobolev loss*, arXiv preprint arXiv:2402.00152, (2024).
- [62] Y. YANG, Y. WU, H. YANG, AND Y. XIANG, *Nearly optimal approximation rates for deep super relu networks on sobolev spaces*, arXiv preprint arXiv:2310.10766, (2023).
- [63] Y. YANG, H. YANG, AND Y. XIANG, *Nearly optimal vc-dimension and pseudo-dimension bounds for deep neural network derivatives*, Advances in Neural Information Processing Systems, 36 (2024).
- [64] D. YAROTSKY, *Error bounds for approximations with deep ReLU networks*, Neural Networks, 94 (2017), pp. 103–114.
- [65] L. ZHANG, T. LUO, Y. ZHANG, Z. JOHN XU, Z. MA, ET AL., *Mod-net: A machine learning approach via model-operator-data network for solving pdes*, Communications in Computational Physics, 32 (2022), pp. 299–335.
- [66] H. ZHENG, Y. HUANG, Z. HUANG, W. HAO, AND G. LIN, *Hompinns: Homotopy physics-informed neural networks for solving the inverse problems of nonlinear differential equations with multiple solutions*, Journal of Computational Physics, 500 (2024), p. 112751.
- [67] D. ZHOU, Y. XIAO, Y. ZHANG, Z. XU, AND D. CAI, *Causal and structural connectivity of pulse-coupled nonlinear networks*, Physical review letters, 111 (2013), p. 054102.